

# SN 2013fs and SN 2013fr: Exploring the circumstellar-material diversity in Type II supernovae

Christopher Bullivant<sup>1★</sup>, Nathan Smith<sup>1</sup>, G. Grant Williams<sup>1,2</sup>, Jon C. Mauerhan<sup>3</sup>, Jennifer E. Andrews<sup>1</sup>, Wen-Fai Fong<sup>1</sup>, Christopher Bilinski<sup>1</sup>, Charles D. Kilpatrick<sup>6</sup>, Peter A. Milne<sup>1</sup>, Ori D. Fox<sup>4</sup>, S. Bradley Cenko<sup>5</sup>, Alexei V. Filippenko<sup>3</sup>, WeiKang Zheng<sup>3</sup>, Patrick L. Kelly<sup>3</sup>, Kelsey I. Clubb<sup>3</sup>

<sup>1</sup>*Steward Observatory, University of Arizona, 933 N. Cherry Ave., Tucson, AZ 85721, USA*

<sup>2</sup>*MMT Observatory, P.O. Box 210065, University of Arizona, Tucson, AZ 85721-0065, USA*

<sup>3</sup>*Department of Astronomy, University of California, Berkeley, CA 94720-3411, USA*

<sup>4</sup>*Space Telescope Science Institute, 3700 San Martin Dr., Baltimore, MD 21218, USA*

<sup>5</sup>*Astrophysics Science Division, NASA Goddard Space Flight Center, Greenbelt, MD 20771, USA*

<sup>6</sup>*Department of Astronomy and Astrophysics, University of California, Santa Cruz, CA 95064, USA*

Accepted XXX. Received YYY; in original form ZZZ

## ABSTRACT

We present photometry and spectroscopy of SN 2013fs and SN 2013fr in the first  $\sim 100$  days post-explosion. Both objects showed transient, relatively narrow  $H\alpha$  emission lines characteristic of SNe IIn, but later resembled normal SNe II-P or SNe II-L, indicative of fleeting interaction with circumstellar material (CSM). SN 2013fs was discovered within 8 hr of explosion; one of the earliest SNe discovered thus far. Its light curve exhibits a plateau, with spectra revealing strong CSM interaction at early times. It is a less luminous version of the transitional SN IIn PTF11iqb, further demonstrating a continuum of CSM interaction intensity between SNe II-P and SNe IIn. It requires dense CSM within  $6.5 \times 10^{14}$  cm of the progenitor, from a phase of advanced pre-SN mass loss beginning shortly before explosion. Spectropolarimetry of SN 2013fs shows little continuum polarization ( $\sim 0.5\%$ , consistent with zero), but noticeable line polarization during the plateau phase. SN 2013fr morphed from a SN IIn at early times to a SN II-L. After the first epoch its narrow lines probably arose from host-galaxy emission, but the bright, narrow  $H\alpha$  emission at early times may be intrinsic to the SN. As for SN 2013fs, this would point to a short-lived phase of strong CSM interaction if proven to be intrinsic, suggesting a continuum between SNe IIn and SNe II-L. It is a low-velocity SN II-L like SN 2009kr, but more luminous. SN 2013fr also developed an infrared excess at later times, due to warm CSM dust that require a more sustained phase of strong pre-SN mass loss.

**Key words:** supernovae: general — supernovae: individual (SN 2013fs, SN 2013fr) — stars: mass-loss — stars: circumstellar matter

## 1 INTRODUCTION

The expected results of core collapse in massive stars are strongly linked to the nature of the progenitor, but connections between progenitor types and supernova (SN) properties remain uncertain. Further complicating matters, spectral and photometric features in a SN are not necessarily linked to the physics of the explosion, because they may be

partly a result of the progenitor’s environment. The Type IIn SN subclass is a particularly stark example. First coined by [Schlegel et al. \(1990\)](#) and found by [Smith et al. \(2011a\)](#) to account for  $\sim 9\%$  of all CCSNe, SNe IIn are characterised by strong, relatively narrow emission lines, with a general lack of broad components ([Filippenko 1997](#)). These narrow lines are not emitted by the SN ejecta; rather, they come from the ionisation of slow, dense circumstellar material (CSM) shed by the progenitor owing to mass loss during its later evolution [Smith \(2014\)](#), and references within). They are often

★ Email: cwbullivant@email.arizona.edu

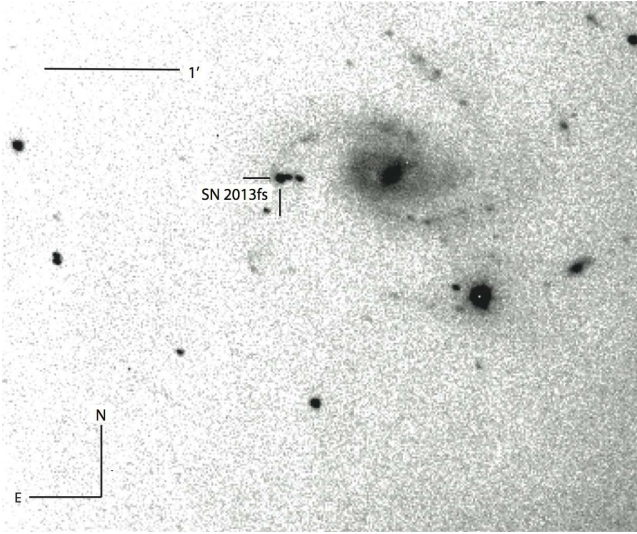


**Figure 1.** Unfiltered image of SN 2013fs taken by KAIT on day 1 (post-discovery;  $\sim 2.5$  days post-explosion). The SN is indicated by the crosshairs, and the image scale is shown on the bottom left.

accompanied by broader lines, a result of shock interaction between the SN ejecta and the dense CSM.

Owing to the fact that mass loss can result from different processes, ranging from pre-SN eruptions to binary interactions or normal radiation-driven winds, SNe IIn are one of the most heterogeneous types of SNe and do not result from a unique class of progenitors. The typical pre-SN mass-loss rates for progenitors that become SNe IIn are greater than  $10^{-4} M_{\odot} \text{ yr}^{-1}$ , and can in some cases be  $1 M_{\odot} \text{ yr}^{-1}$  or more, for superluminous SNe IIn (SLSNe IIn) and even some normal SNe IIn (Smith 2014). Such extreme mass loss is unlikely to be generated by the steady, radiation-driven winds associated with evolved supergiants. Among the most promising ways to achieve such high mass-loss rates is eruptive pre-SN instability in evolved supergiant stars, known to occur in luminous blue variables (LBVs) such as  $\eta$  Carinae (with a very high total ejecta mass  $> 10 M_{\odot}$ ; Smith et al. 2003) and P Cygni (with a more modest ejecta mass of  $\sim 0.1 M_{\odot}$ ; Smith & Hartigan 2006). Eruptive instability has been proposed to explain SNe IIn before (Smith & Owocki 2006), and an erupting LBV becoming a SN IIn has likely been observed in at least one case (e.g., the 2012 outburst of SN 2009ip; Mauerhan et al. 2013); massive stars becoming SNe Ibn shortly after leaving the LBV phase have been observed as well (Foley et al. 2007).

While SNe IIn represent the most extreme pre-SN mass loss, some normal SNe also show signs of strong winds or eruptions. Those classified as SNe IIn throughout their entire evolution have a total CSM in the range  $0.1\text{--}1 M_{\odot}$  for normal SNe IIn, and as much as  $10\text{--}20 M_{\odot}$  or more for SLSNe IIn (Smith 2014). Smith et al. (2015) argued that the degree of mass loss required to generate the characteristic features of SNe IIn extends to lower mass-loss rates, and that some SNe II would be classified as SNe IIn *only if discovered sufficiently early after explosion*, evolving into other types (SNe II-P, SNe II-L) as they age.

Some young SNe display transient Wolf Rayet (WR)-like high-ionisation emission lines, present only if discov-

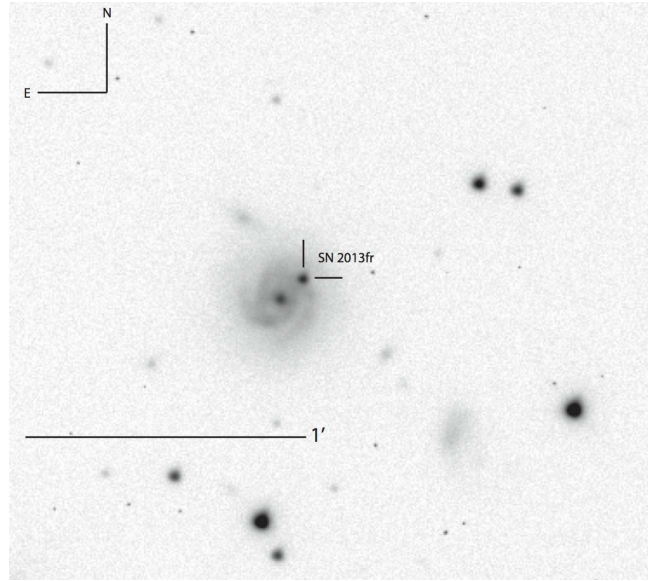


**Figure 2.** *R*-band Lick Nickel telescope image of SN 2013fr, obtained 10 days post-discovery. The SN is indicated by the crosshairs, and the image scale is shown on the bottom left.

ered *very* early (less than a week post-explosion). The earliest such example was reported for SN 1983K by Niemala, Ruiz, & Phillips (1985), and this was followed a decade afterward by Benetti et al. (1994), who observed the same lines in early-time spectra of SN 1993J. The cause of these lines has been interpreted in different ways by different authors. Early papers regarded the He II  $\lambda 4686$  in particular as likely the result of highly blueshifted H $\beta$  emission. Later, Quimby et al. (2007) describe them as the result of X-rays coming from the shock breakout (SBO) and subsequent shock interaction between the SN ejecta and CSM. Most recently, Gal-Yam et al. (2014) and Khazov et al. (2016) ascribe them to the post-SBO ultraviolet (UV) flash.

Leonard et al. (2000) reported both early narrow lines and a high degree of continuum polarization in SN 1998S, interpreting the polarization as evidence for asphericity; Shivvers et al. (2015) later published an even earlier spectrum of SN 1998S, finding the WR-like lines to be stronger. These lines have been observed in several SN types: Quimby et al. (2007) found them in SN 2006bp (II-P), and later Gal-Yam et al. (2014) and Smith et al. (2015) identified these features in SN 2013cu (Iib) and PTF11iqb (IIn). Gal-Yam et al. (2014) proposed, based on the similarity of the spectral features to those of a WN6h spectral type, that SN 2013cu resulted from the explosion of a star having some characteristics of a WR star. However, subsequent work (Groh 2014; Smith et al. 2015) ruled out a WR progenitor, finding that an LBV or yellow hypergiant was more likely. In the last year, Khazov et al. (2016) concluded that early, rapidly fading narrow spectral lines could appear in up to 18% of young SNe. Most of these objects are classified as SNe Iib or SNe IIn, with few known SNe II-P showing such lines.

The existence of any intrinsic distinction between SNe II-P and II-L has been a subject of debate (Fillippenko 1997; Arcavi et al. 2012; Sanders et al. 2015; Valenti et al. 2016; Anderson et al. 2014). Spectroscopically, SNe II-L of-

ten show weaker P Cygni and Ca II absorption than SNe II-P, which may be evidence of CSM interaction in the former due to reionisation of the outer SN ejecta (Smith et al. 2015). Adding to the observational evidence, recent hydrodynamical models by Morozova, Piro, & Valenti (2017) find that the light curves of SNe II-P and II-L can be fit well by RSGs with dense CSM.

In this paper we present optical photometry and spectroscopy of SN 2013fs (shown in Figure 1) and SN 2013fr (shown in Figure 2). Both of these objects showed narrow H $\alpha$  emission at early times, and were initially classified as SNe IIn, but the narrow component caused by CSM interaction later weakened or even disappeared.

SN 2013fs (additional designations: iPTF13dqy and PSN J23194467+1011045) was discovered at  $R = 16.5$  mag by the Itagaki Astronomical Observatory on 2013 Oct. 7.468 (UT dates are used throughout this paper) in an outer spiral arm of NGC 7610 (Nakano et al. 2013). Based on the host-galaxy redshift of  $z = 0.01178$  (3554 km s $^{-1}$ ; NED<sup>1</sup>) and five-year WMAP parameters Komatsu et al. (2009), we adopt a distance of  $50.6 \pm 0.9$  Mpc ( $m - M = 33.52 \pm 0.04$  mag) with  $E(B - V) = 0.0347$  mag (Schlafly & Finkbeiner 2011). SN 2013fs is located 49'' east and 2'' south of the host nucleus (separation  $\sim 12$  kpc), and was initially classified as a probable SN IIn based on a spectrum obtained on 2013 Oct. 8 (day 1). SN 2013fs was reclassified on 2013 Oct. 24 (day 17) with additional WiFeS data as a SN II-P, with SNID (Blondin & Tonry 2007) providing a best match to SN 1999em (Childress et al. 2013).

SN 2013fr was discovered at  $I = 16.2$  mag by the Catalina Sky Survey on 2013 Sep. 28.42 at a projected separation of  $\sim 6.7''$  ( $\sim 2.5$ – $3$  kpc) from the nucleus of MCG+04-10-24, in an inner spiral arm. Initially designated as PSN J04080235+2317394, SN 2013fr was classified as a SN IIn using spectra from the F. L. Whipple Observatory 1.5 m telescope obtained on day 1 (Howerton et al. 2013). Based on the host  $z = 0.020941$  (6278 km s $^{-1}$ ) from NED and five-year WMAP parameters Komatsu et al. (2009), we adopt a distance of  $87.0 \pm 1.6$  Mpc ( $m - M = 34.70 \pm 0.04$  mag) with  $E(B - V) = 0.2308$  mag (Schlafly & Finkbeiner 2011). This yields a discovery  $I$ -band absolute magnitude of  $-18.48$ .

## 2 OBSERVATIONS AND DATA

### 2.1 SN 2013fs<sup>2</sup>

#### 2.1.1 Lick KAIT/Nickel photometry

After each discovery, both SNe were observed by the Katzman Automatic Imaging Telescope (KAIT; Filippenko et al. 2001) at Lick Observatory. KAIT obtained photometry of SN 2013fs in the clear filter for 61 epochs from 0 to 109 days post-discovery, and 26 epochs of *BVRI* photometry from 3 to 49 days post-discovery. No source was detected at the

location of SN 2013fs on 2013 Oct. 05.27 (two days pre-discovery) down to a  $3\sigma$  unfiltered limit  $\sim 19.24$  mag. The resulting data are listed in Table 2 for the filtered photometry and Table 3 for the unfiltered photometry.

KAIT photometry of SN 2013fr covers 9 epochs from day 22 to day 58 in the *BVRI* filters, and the Nickel telescope at Lick observed SN 2013fr for 8 epochs in the same filters; these data are listed together in Table 4. All photometry is corrected for Milky Way line-of-sight extinction  $E(B - V) = 0.0347$  mag (Schlafly & Finkbeiner 2011).

The data was reduced with the KAIT standard photometry pipeline Ganeshalingam et al. (2010), using template subtraction to remove host galaxy contamination, aperture photometry using Landolt standards is used to calibrate to the standard photometry system. All KAIT/Nickel data are reported on the Vega system.

#### 2.1.2 Kuiper photometry

Four epochs of late-time *BVRI* photometry of SN 2013fs were obtained by the AZTEC (Arizona Transient Exploration and Characterization) collaboration with the Kuiper 61 inch telescope on Mt. Bigelow, using the Mont4k CCD at the  $f/13.5$  Cassegrain focus, and a  $9.73' \times 9.73'$  field of view with  $0.42''$  pixel $^{-1}$ . The seeing ranged between  $1''$  and  $2''$ . No source was detected at the location of the SN; limiting magnitudes were obtained using the method described by Bilinski et al. (2015). The late-time data are given in Table 5.

#### 2.1.3 Swift UVOT photometry

After discovery, SN 2013fs was added to the queue for the UltraViolet and Optical Telescope (UVOT) aboard *Swift* (Roming et al. 2005), and observed for 21 epochs with all filters. The base UVOT data were taken from the *Swift* Optical/Ultraviolet Supernova Archive (Brown et al. 2014). We obtained a template image of NGC 7610 on 2016 July 14, and the data were reduced using the method of Brown et al. (2009), subtracting host-galaxy count rates and using the revised UV zeropoints and time-dependent sensitivity from Breeveld et al. (2011). The resulting photometry is shown in Table 7.

#### 2.1.4 Spectroscopy

Eight low-to-moderate resolution spectra and one higher-resolution spectrum covering the first 87 days post-explosion were obtained of SN 2013fs, and they are supplemented with additional archival spectra (see Section 2.3.2). Three spectra were obtained during the first week using the SPol spectropolarimeter on the Kuiper telescope, two on days 21 and 23 using SPol at MMT Observatory, and three more between days 52 and 86 with SPol on the 2.1 m Bok telescope. One high-resolution spectrum was taken on day 87 using the Bluechannel spectrograph at the MMT. The technical details of these observations appear in Table 8.

All spectra were reduced using standard reduction techniques as described by Foley et al. (2003) and references therein. Wavelength calibration was done at the 2.1 m Bok, 61'' Kuiper, and 6.5 m MMT telescopes using a HeNeAr

<sup>1</sup> NED: The NASA/IPAC Extragalactic Database (NED) is operated by the Jet Propulsion Laboratory, California Institute of Technology, under contract with the National Aeronautics and Space Administration (NASA).

<sup>2</sup> Some facilities obtained data for both SNe. In these cases, the data obtained with those facilities are mentioned in this section only.

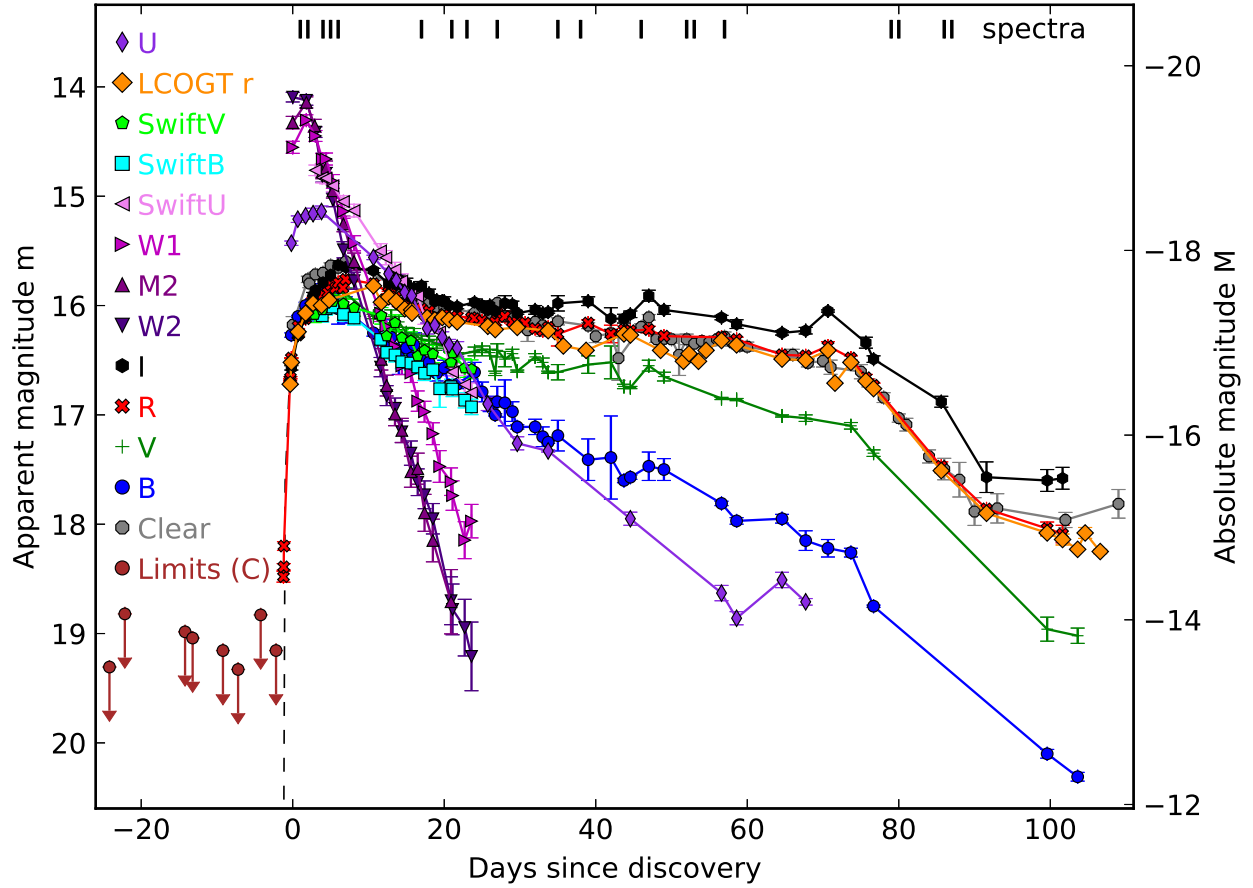


**Figure 3.** All early-time UV and optical light curves of SN 2013fs. The unfiltered data in grey are roughly the photometric equivalent of an  $R$  filter. All photometry have been corrected for Milky Way reddening with  $E(B - V) = 0.0347$  mag, from [Schlafly & Finkbeiner \(2011\)](#). Magnitudes are reported on the Vega system.

lamp, and flux calibration using spectra of standard stars taken on the night of the observations.

### 2.1.5 Spectropolarimetry

As part of the Supernova Spectropolarimetry (SNSPOL) Project<sup>3</sup>, we observed SN 2013fs during four epochs using the CCDImaging/Spectropolarimeter ([Schmidt et al. 1992](#)) mounted on either the 61 inch Kuiper, 6.5 m MMT, or 90-inch Bok telescopes. These correspond to the days 4–6, day 21/23, and days 52, 57, and 86 spectra in the top half of Table 8, respectively. At the 90 inch and 61 inch telescopes, we used a  $3.0''$  slit with the  $600 \text{ lines mm}^{-1}$  grating blazed at  $11.35^\circ$  ( $5819 \text{ \AA}$ ). This configuration provides a spectral coverage of  $4970 \text{ \AA}$  at a full-width at half-maximum intensity (FWHM) resolution of  $19.5 \text{ \AA}$ . At the MMT we used either a  $1.9''$  slit or a  $2.8''$  slit with the  $964 \text{ lines mm}^{-1}$  grating. This configuration provides a spectral coverage of  $3140 \text{ \AA}$  with a resolution of  $19.8 \text{ \AA}$  ( $1.9''$  slit) or  $29.1 \text{ \AA}$  ( $2.8''$  slit).

Effects of pixel-to-pixel variations are reduced by obtaining a pair of exposures with the ordinary and extraordinary traces swapped on the detector for both linear Stokes parameters,  $(Q_1, Q_2)$  and  $(U_1, U_2)$ . During data reduction, those exposures are combined into a single  $Q$  image and a single  $U$  image. To reduce variations caused by waveplate orientation, each exposure is an integration over four equivalent waveplate rotation angles as follows:

$$\begin{aligned} Q_1 &: 67.5^\circ, 157.5^\circ, 247.5^\circ, 337.5^\circ \\ Q_2 &: 22.5^\circ, 112.5^\circ, 202.5^\circ, 292.5^\circ \\ U_1 &: 45^\circ, 135^\circ, 225^\circ, 315^\circ \\ U_2 &: 0^\circ, 90^\circ, 180^\circ, 270^\circ \end{aligned} \quad (1)$$

During each observing run we obtained a standard set of calibration data which include He-Ne-Ar comparison-lamp spectra and flatfield spectra for every slit. To measure and correct for the polarimetric efficiency of the instrument, we also obtained a full  $Q, U$  sequence of a continuum source through a nicol prism. Observations of unpolarized flux standards (BD+28 4211 and G191-B2B) and polarized standards (Hiltner 960, VI Cyg #12, BD+59 389, and HD 245310) were acquired multiple times during each observing run. The po-

<sup>3</sup> <http://grb.mmt.arizona.edu/~ggwilli/snsopol/>

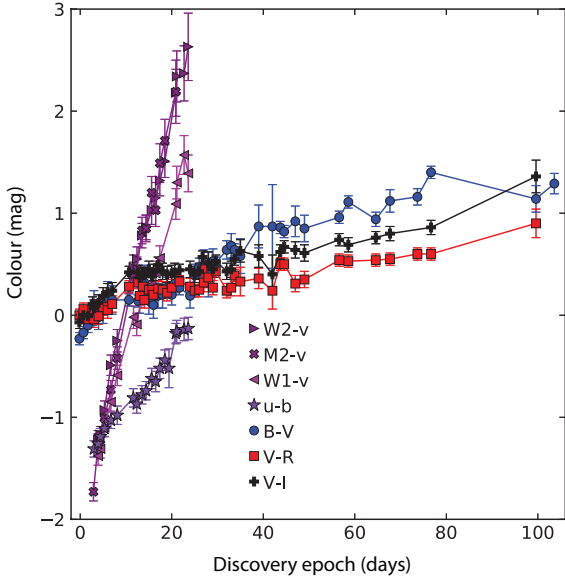


**Figure 4.** Colour evolution of SN 2013fs. The  $B-V$ ,  $V-R$ , and  $V-I$  evolution is largely flat with time. All photometry has been corrected for Milky Way reddening with  $E(B - V) = 0.0347$  mag.

larized standards are used to calibrate the polarization position angle.

The raw data were bias subtracted and flatfielded in a standard way. Polarimetric reduction was carried out using custom-made IRAF scripts. All the  $Q$  and  $U$  spectra obtained during a given observing run were coadded to improve the signal-to-noise ratio (S/N).

We calculate  $P$  and  $\theta$  from  $Q$  and  $U$  using the debiasing prescription of [Wardle & Kronberg \(1974\)](#):

$$P = \pm \sqrt{|Q|^2 + U^2 - \frac{1}{2}(\sigma_Q^2 + \sigma_U^2)}, \quad (2)$$

$$\theta = \frac{1}{2} \tan^{-1}(U/Q). \quad (3)$$

The sign of  $P$  is chosen based on the sign of the result in the absolute-value operator.

## 2.2 SN 2013fr

### 2.2.1 RATIR photometry

We obtained 18 epochs (days 7–76) of photometry of SN 2013fr using the multi-channel Reionization And Transients InfraRed camera (RATIR; [Butler et al. 2012](#)) mounted on the 1.5 m Johnson telescope at the Mexican Observatorio Astronómico Nacional on Sierra San Pedro Mártir in Baja California, México ([Watson et al. 2012](#)). Typical observations include a series of 80 s exposures in the  $ri$  bands and 60 s exposures in the  $ZYJH$  bands, with dithering between exposures. Given the lack of a cold shutter in RATIR’s design, infrared (IR) dark frames are not available. Laboratory testing, however, confirms that the dark current is negligible in both IR detectors ([Fox et al. 2012](#)).

The data were reduced, coadded, and analysed using standard CCD and IR processing techniques in IDL and Python, utilising online astrometry programs **SExtractor**

and **SWarp**<sup>4</sup>. The photometry in the Sloan Digital Sky Survey (SDSS)  $r$  filter for the nights between day 27 and 59 for which there is overlap with the KAIT/Nickel Johnson-Cousins  $R$  photometry show a slightly smaller rate of decline in the former. These data are given in Table 6.

### 2.2.2 DCT photometry

One epoch of SN 2013fr photometry was obtained on day 139 using the Large Monolithic Imager (LMI) mounted on the 4.3 m Discovery Channel Telescope, in the SDSS  $g$ ,  $r$ , and  $i$  filters; no source was visible down to 23.29, 23.80, and 23.04 mag (respectively). The photometry was obtained in the same way as the Kuiper photometry, and these deep upper limits set strong limits on the later light-curve decline rate (and possible plateau drop), as discussed in Sections 3.2.1 and 5.

### 2.2.3 Spectroscopy

Seven low-resolution spectra were obtained using the Kast spectrograph on the 3 m Shane telescope at Lick Observatory ([Miller & Stone 1993](#)), and one low-resolution spectrum was obtained on day 46 using the IMACS spectrograph on the Baade Magellan telescope at Las Campanas Observatory ([Dressler et al. 2011](#)) with the 300 line  $\text{mm}^{-1}$  grating. All spectra are from the first 69 days post-explosion, and have been corrected for redshift using the DOPCOR package in IRAF, and dereddened assuming  $R_V = 3.1$ . The spectral evolution in the first 69 days is the subject of Section 3.2.2, and technical information on the instruments used to obtain these data is given in the bottom half of Table 8.

## 2.3 Archival data

### 2.3.1 Archival photometry

The KAIT, *Swift*, and Kuiper photometry of SN 2013fs was supplemented with  $r$  and  $R$  band photometry obtained from the Open Supernova Catalogue (OSC) ([Guillochon, Parrent, & Margutti. 2016](#))<sup>5</sup>. The  $r$  and  $U$ -band data, as well as all of the  $BVRI$  photometry after day 49 post-discovery, were obtained from the Las Cumbres Observatory Global Telescope Network (which observed SN 2013fs for 39 epochs covering days 0 to 106 after discovery. The  $R$ -band data come from the PTF48 telescope at Mount Palomar for the first week post-explosion. All archival photometry was added to the OSC by [Valenti et al. \(2016\)](#) after use in their paper exploring correlations between SN II diversity and possible progenitors.

### 2.3.2 Archival spectroscopy

The spectra obtained by Lick/Kast, Bok, Kuiper, Magellan, and MMT were supplemented by data obtained from online archives. For SN 2013fs, we obtained seven low-resolution spectra covering days 2 through 80, and four

<sup>4</sup> SExtractor and SWarp can be accessed from <http://www.astromatic.net/software>.

<sup>5</sup> <https://sne.space>

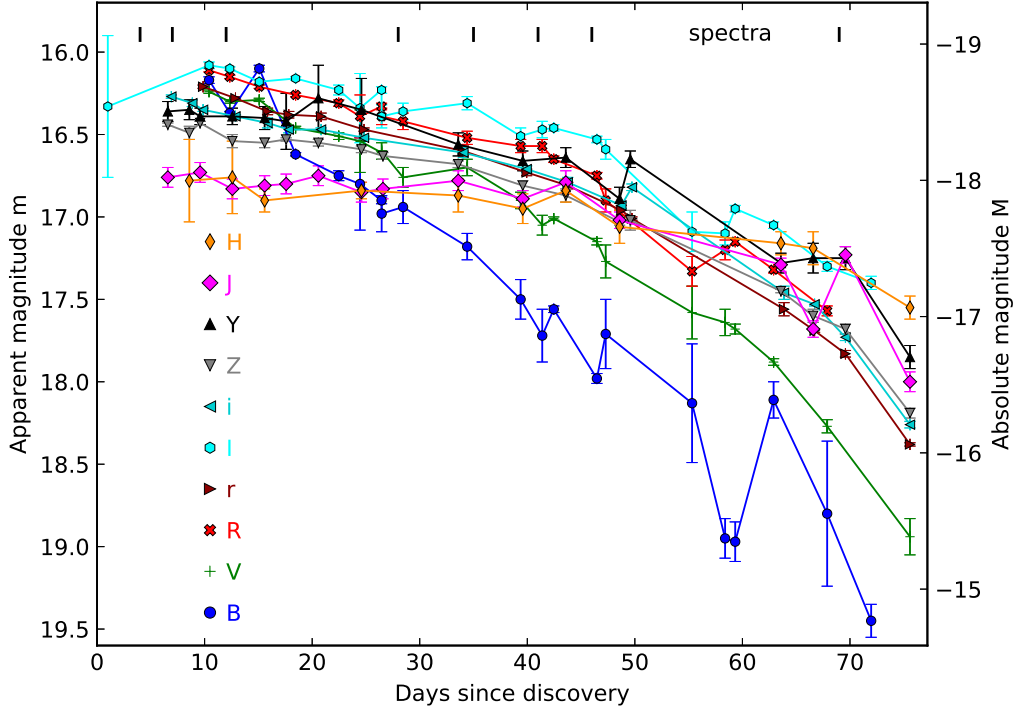


**Figure 5.** Optical and near-infrared light curves of SN 2013fr. The BVRI photometry is on the Vega system, and the rizYJH have been converted to the AB system. All points in this plot have been corrected for Milky Way reddening with  $E(B - V) = 0.2076$  mag, from Schlafly & Finkbeiner (2011).

moderate-resolution spectra from days 1 to 52 via WIS-eREP (Yaron & Gal-Yam 2012). The low-resolution spectra come from the Public ESO Spectroscopic Survey of Transient Objects (PESSTO; Smartt et al. (2015)), who obtained them using the Faint Object Spectrograph on the European Southern Observatory (ESO) New Technology Telescope (NTT). The PESSTO spectra at days 27, 35, 46, and 53, originally split into two spectra, have been merged around  $5500 \text{ \AA}$  (the [O I] night-sky emission line was removed from these spectra). The moderate-resolution spectra come from the Australian National University (ANU) Wide-Field Spectrograph (WiFeS) SuperNova Program (AWSNAP) (Childress et al. 2016). These spectra were originally used to reclassify SN 2013fs as a SN II-P (Childress et al. 2013). The first WiFeS spectrum, taken within 48 hr of the initial explosion, is one of the earliest spectra obtained of a young SN, and is a direct probe of the CSM very close to the explosion site; this is discussed in Section 4.

For SN 2013fr, a single, day 4 PESSTO spectrum with a resolution of  $5.4 \text{ \AA}$  was obtained from WIS-eREP.

### 3 RESULTS

#### 3.1 SN 2013fs

##### 3.1.1 Pre-discovery photometry & Swift UVOT light curves

SN 2013fs was discovered extremely young, within 48 hr of the explosion based on the time between the last KAIT upper limit and the discovery by Nakano et al. (2013), and was detected within 8 hr based on the pre-discovery  $R$ -band photometry the day before (making SN 2013fs one of the only SNe detected so soon after explosion). As the initial rise to maximum is often proportional to  $t^2$  Smith et al. (2015), we fit the early-time  $R$ -band light curve (in magnitudes) to a quadratic function of the form  $a(t - t_0)^2$  (plotted as the dashed line in Figure 3). The fit suggests that the explosion occurred 1.5 days before discovery, on 2013 Oct. 5.946 (MJD 56570.946) ( $\pm 0.2$  days), consistent with the KAIT upper limits. Follow-up observations began almost immediately with both KAIT and *Swift* UVOT. All photometry of SN 2013fs, including the eight most recent pre-discovery upper limits, is plotted in Figure 3; owing to the lack of a resolved sodium doublet in the spectra, host-galaxy reddening is presumed to be negligible. The UV light curve of SN 2013fs is similar to the typical light curves of some SNe II-n and most SNe II-P, rapidly fading linearly in the  $UVW2/UVW1$  filters, and more slowly (but still linearly) in the  $u$  filter. The  $b$  and  $v$  filters trace the KAIT  $B$  and  $V$  filters fairly well, though

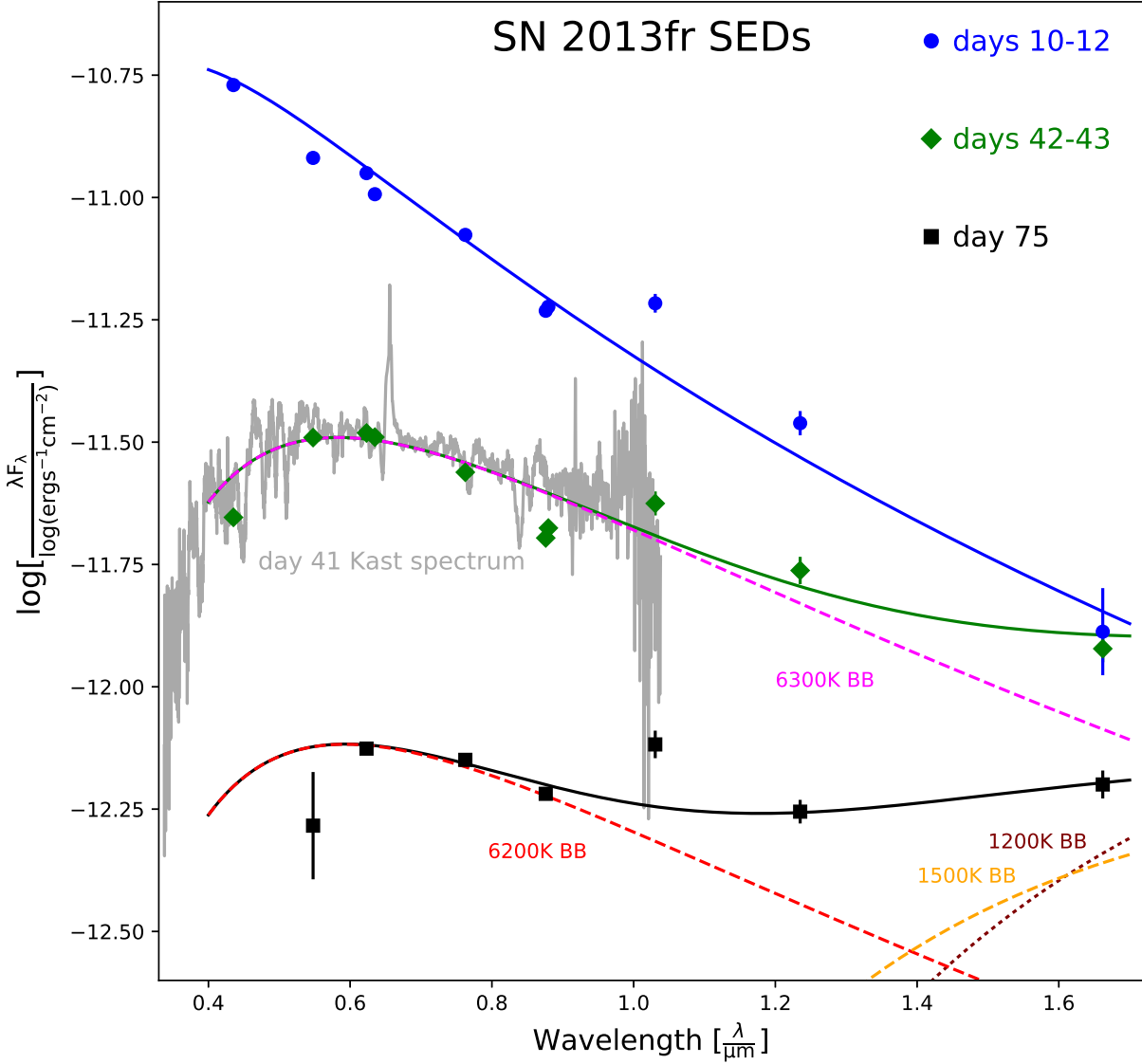


**Figure 6.** SEDs of SN 2013fr for days 10–12 (blue), days 42/43 (green), and day 75 (black) post-discovery. Each SED has an associated blackbody function having the same colour: single temperature for the first SED, and double temperature for the others. The  $Y$ -band photometry at  $1\ \mu\text{m}$  is calibrated to the UKIDSS  $Y$  band, which may have caused a systemic shift in brightness. All points are calibrated for Milky Way reddening ( $E(B - V) = 0.2076\ \text{mag}$ ).

brighter by  $< 0.1\ \text{mag}$  after the KAIT magnitudes were corrected for extinction.

Unlike many other SNe, the fast follow-up observations of SN 2013fs managed to catch a small rise in the  $UVM2$  and  $UVW1$  filters:  $-0.185$  and  $-0.249\ \text{mag}$ , respectively. Over this period, the  $UVW2$  filter recorded only a  $0.029\ \text{mag}$  decline, suggesting that its maximum was reached very quickly, within 24 hr of the explosion (by contrast, the  $UVM2$  and  $UVW1$  bands peak around 70 hr post-explosion). The maxima in the  $UVW2/UVM2/UVW1$  bands range from

$-19.14$  to  $-19.35$ , and the average decline in those bands is  $0.23/0.24/0.17\ \text{mag day}^{-1}$ , consistent with the mean decline rates for SNe II-P (Pritchard et al. 2013).

Comparison with the UV light curves of several SNe from Pritchard et al. (2013) (in this analysis, we look solely at the subset of SNe II-P/II<sub>n</sub> featured in Figure 6 of Pritchard et al. (2013), as only this subset of their sample has derived explosion dates; we ignore SN 2008am and SN 2008es, as these are SLSNe) and the SN II-P SN 2014cx Huang et al. (2016) show that SN 2013fs is very similar to

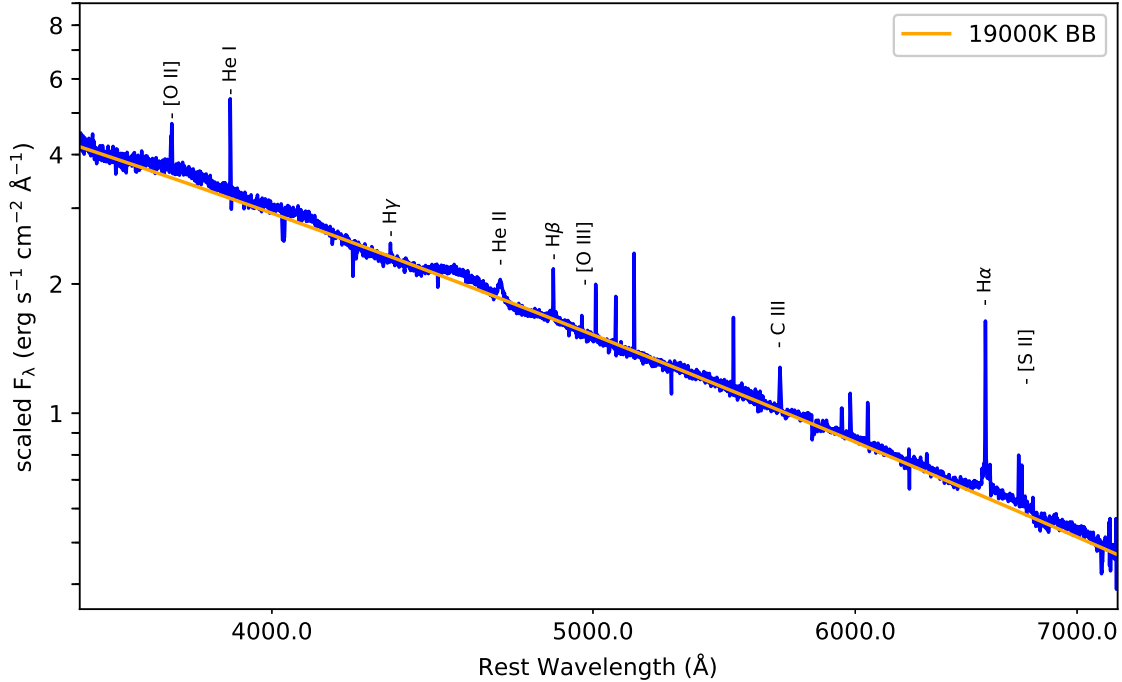


**Figure 7.** Day 1 (post-discovery) spectrum of SN 2013fs overplotted with a 19,000 K blackbody, with spectral features of interest marked. The spectrum has been dereddened and redshift corrected. We suspect that the unmarked narrow features from  $\sim 5000\text{--}6000\text{\AA}$  are telluric sky lines that were incompletely subtracted; they are all narrow and unresolved, and they coincide with wavelengths of expected sky lines. Further, they do not match the wavelengths of narrow emission lines seen in other SNe II P discovered early.

other SNe II-P at similar epochs, though brighter than average in the *UVW2/UVW1* filters. The Milky Way reddening ( $E(B-V)$ ) for the full sample is less than 0.06 in all but one case (it is 0.09 for SN 2014cx). SN 2013fs is brighter in the *UVW2/UVW1* filters than every other SN II-P in our sample at early times, usually by more than a magnitude. The only brighter SN is SN 2007pk, the sole SN IIn in Pritchard et al. (2013) the sample. No host reddening is available for most of these SNe, and so this excess brightness may be the result of higher host reddening in the sample SNe. SN 2006bp in particular, has a very high host reddening of  $E(B-V) = 0.37$  mag (from Table 2 in Pritchard et al. 2013). This is noteworthy because SN 2006bp is the only SNe II-P in sample set known to have had WR-like emission lines at early times, and at a difference of 2.7 mag in the *UVW2* filter, it is the second dimmest SN II-P in the sample set.

The *UV-v* colour curves of SN 2013fs plotted in Figure 4 behave like those of a typical SN II-P; they start out extremely blue, and rapidly redden with time. Most SNe II-P settle into a UV plateau around 20 days after *v*-band maximum, and the reddening levels off. This may be beginning to happen in the *UVW1-v* colour on the last epoch of UVOT observations, but it is not seen in *UVW2* and *UVM2*. It would be tempting to say that this indicates a deviation from the typical UV colour evolution of a SN II-P, were it not for the fact that at late times host contamination in the

deeper UV filters is not negligible and can cause up to a 1 mag difference in the photometry.

### 3.1.2 Optical light curves

As with the UV photometry, SN 2013fs peaks in the optical very quickly after discovery, reaching a *B*-band maximum  $M_B = -17.66$  mag and a *V*-band maximum  $M_V = -17.69$  mag on days 4 and 6 after the discovery. After peak, it settles into the plateau phase with a luminosity around  $M_R = -17.50$  mag, where it remains for at least 50 days. The unfiltered, *r*, and *BVRI* photometry show that the plateau drops off around day 75, dimming by more than a magnitude in the *r/R* filters over the next 34 days, after which our photometric coverage ends.

SN 2013fs exhibits a shorter plateau relative to many SNe II-P (by about a month), and a brief, sharp peak in the early light curve not seen in most SNe II-P. Detailed comparison of SN 2013fs with the interacting Type IIn SN 1998S, the gap-bridging SN IIn PTF11iqb, and the archetypal Type II-P SN 1999em is the subject of Section 4.

### 3.1.3 Spectral evolution

SN 2013fs was initially classified as a young SN IIn, owing to the narrow  $H\alpha$  emission in the first epoch. The day 1 spectrum in Figure 7 exhibits a blue continuum with narrow lines, with hydrogen emission features and He II  $\lambda 4686$

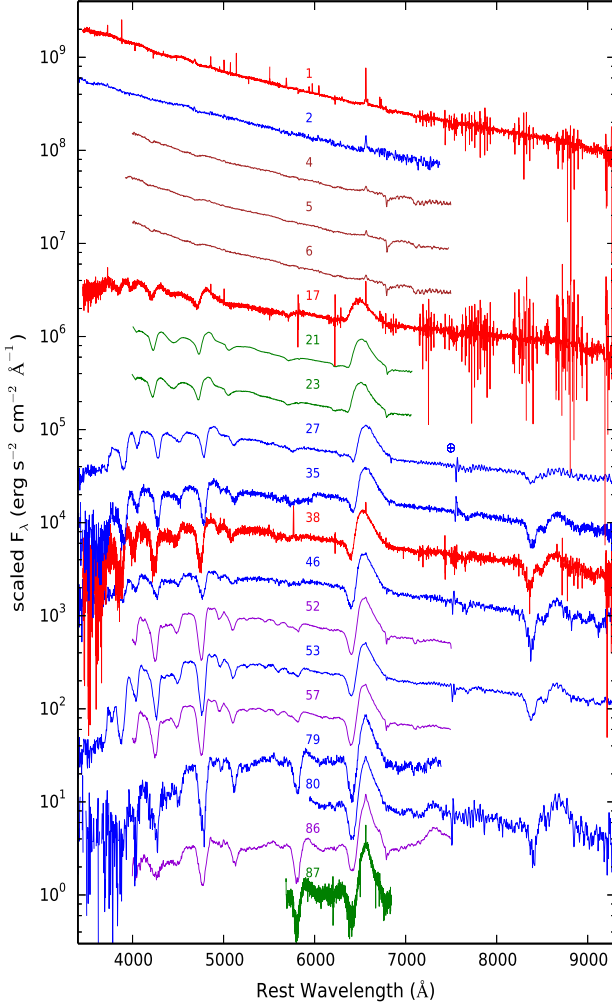


**Figure 8.** Spectra of SN 2013fs, corrected for Milky Way reddening, from WiFeS (red), PESSTO (blue), Kuiper (brown), Bok (purple), and the MMT (green).  $\oplus$  markings indicate uncorrected telluric absorption.

having a broad blueshifted base with  $\text{FWHM} \approx 11,500 \text{ km s}^{-1}$ , and a narrower component with Lorentzian wings and  $\text{FWHM} \approx 1000 \text{ km s}^{-1}$ . This has been observed in a handful of SNe for which very early spectra are available, including SN 1998S (Shivvers et al. 2015), SN 2006bp (Quimby et al. 2007), SN 2013cu (Gal-Yam et al. 2014), and PTF11iqb (Smith et al. 2015). Similar to SN 2006bp and dissimilar to SN 1998S, SN 2013cu, and PTF11iqb, only He II is distinguishable, while the common C III/N III  $\lambda 4640$  line is either very weak or absent. Deblending the emission line using Lorentzian fits shows that if there is a distinct emission line at  $4640 \text{ Å}$ , then the C III/N III line is weaker than He II; the equivalent width (EW) ratio  $\text{EW}(\lambda 4640)/\text{EW}(\lambda 4686) \lesssim 0.08$ .

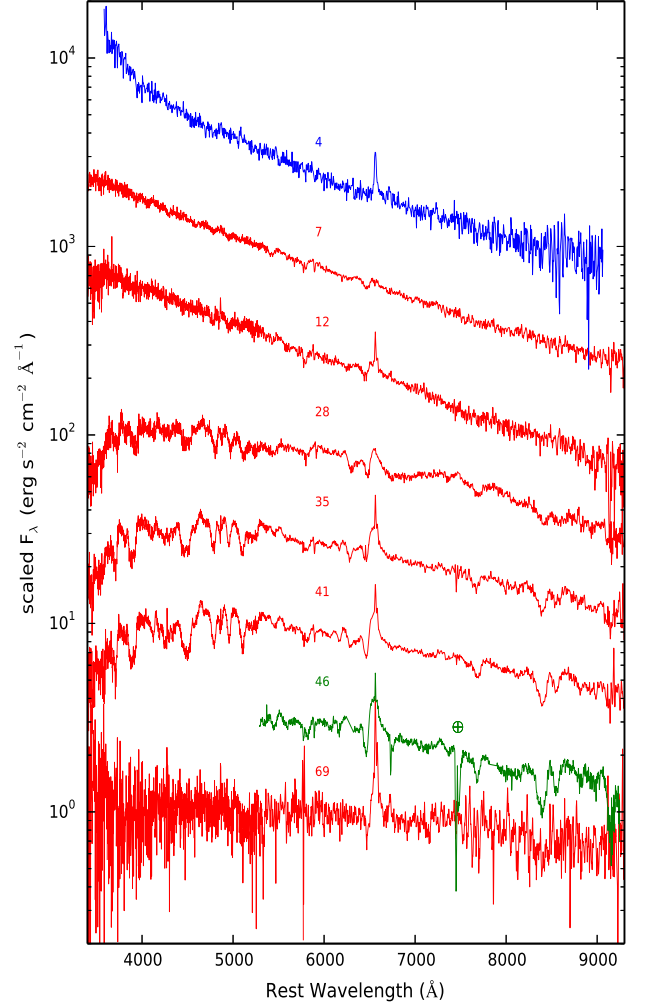


**Figure 9.** All spectra of SN 2013fr, corrected for Milky Way reddening. Red spectra are from the Lick Shane telescope, green from Magellan, and blue from PESSTO; the  $\oplus$  marks indicate uncorrected telluric absorption.

All spectra of SN 2013fs are plotted in Figure 8. The narrow  $H\alpha$  persists for at least a week post-discovery. The line profile broadens by day 17 and develops a standard P Cygni profile, typical of normal SNe II-P. The moderate-resolution spectra indicate that a small narrow component remains, and other narrow features in Figure 7 are indicative of an H II region. Using the moderate-resolution MMT spectrum and WiFeS spectra, the  $H\alpha$  line profile of SN 2013fs is plotted on the left side of Figure 10. The  $H\alpha$  profile on day 1 has faint [N II] emission. These features fade as the P Cygni profile develops, and the velocity of the absorption trough becomes increasingly redshifted from day 17 to 87. After the plateau drop, the P Cygni absorption becomes narrower, with  $\text{FWHM} \approx 3900 \text{ km s}^{-1}$ .

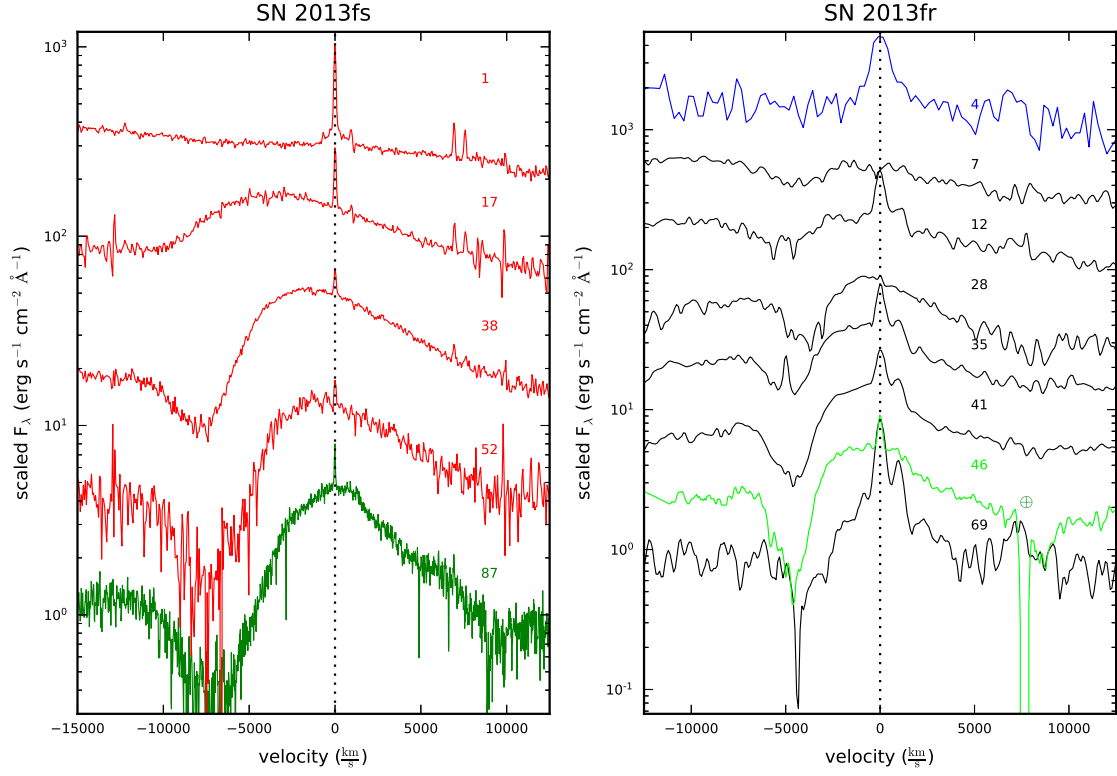


**Figure 10.**  $H\alpha$  line profile of both SNe; SN 2013fs is on the left, SN 2013fr on the right. Telluric features are marked with  $\oplus$ . Spectra are from WiFeS (red), MMT (dark green), PESSTO (blue), Lick/Shane (black), and Magellan (light green).

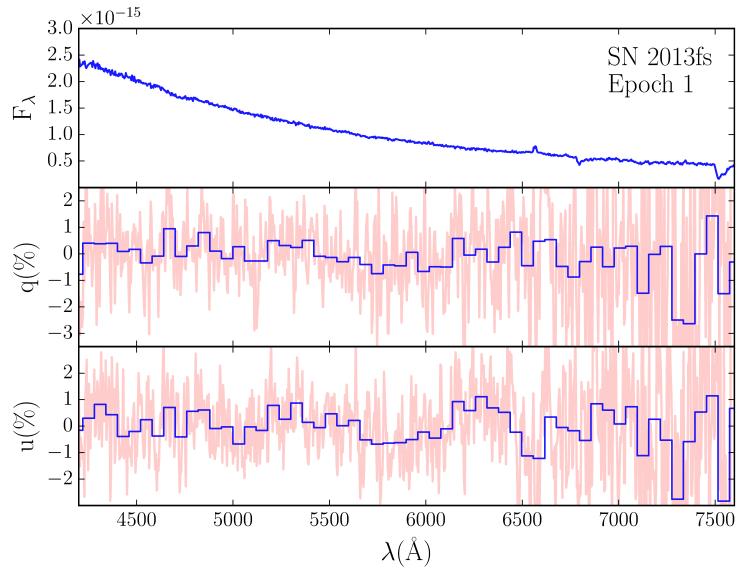


**Figure 11.** Kuiper spectropolarimetry of SN 2013fs, days 4–6 post-discovery.

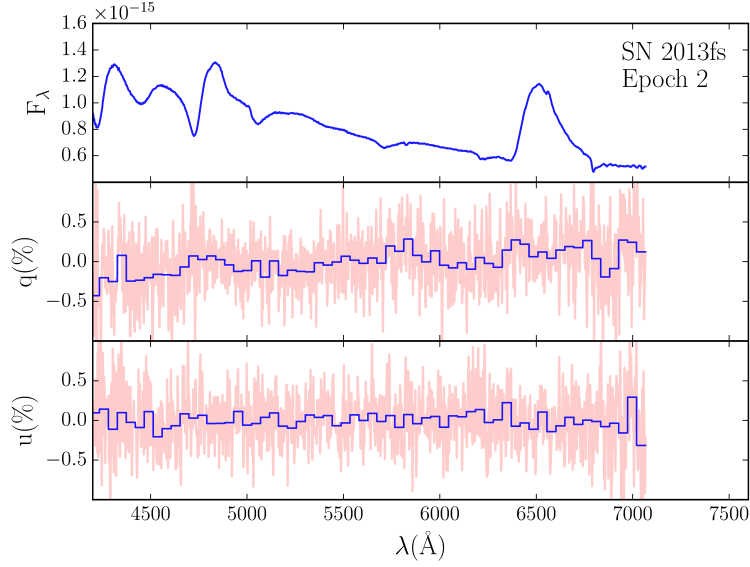


**Figure 12.** MMT spectropolarimetry of SN 2013fs, days 21 and 21 post-discovery.

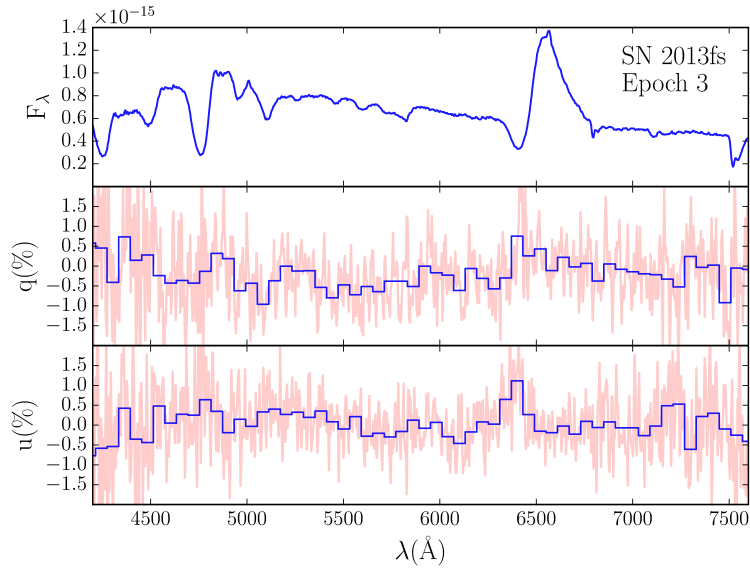


**Figure 13.** Bok spectropolarimetry of SN 2013fs, days 52 and 57 post-discovery.

### 3.1.4 Spectropolarimetric evolution

Establishing an accurate interstellar polarization (ISP) is often necessary to properly interpret the polarimetric results. Here, we determine an ISP value by assuming the intrinsic polarization of our Epoch-2 data (i.e., the data with the highest S/N; days 21 and 23 post-discovery) is zero or centred around  $(q, u) = (0, 0)$ . This assumption may be incorrect, but a different ISP value will not alter our interpretation significantly. Therefore, we adopt the inverse-variance weighted averages over the full spectra for Epoch 2

of  $(q, u) = (-0.45, -0.26)$  as the ISP value. All the figures show only ISP-subtracted data.

Figures 11 through 14 show the scaled  $F_\lambda$ , and normalised linear Stokes parameters  $q$  and  $u$  as a function of wavelength for the four epochs as specified in Section 2.1.5. The unbinned  $q$  and  $u$  data are shown in light red and data binned by 15 pixels is overplotted in blue. The flux data are always unbinned. Figure 15 shows the binned data from all four epochs plotted in the  $(q, u)$  plane colour coded by wavelength. The low-S/N data below 4200 Å are not plotted. The light-grey crosshairs show the position of the origin

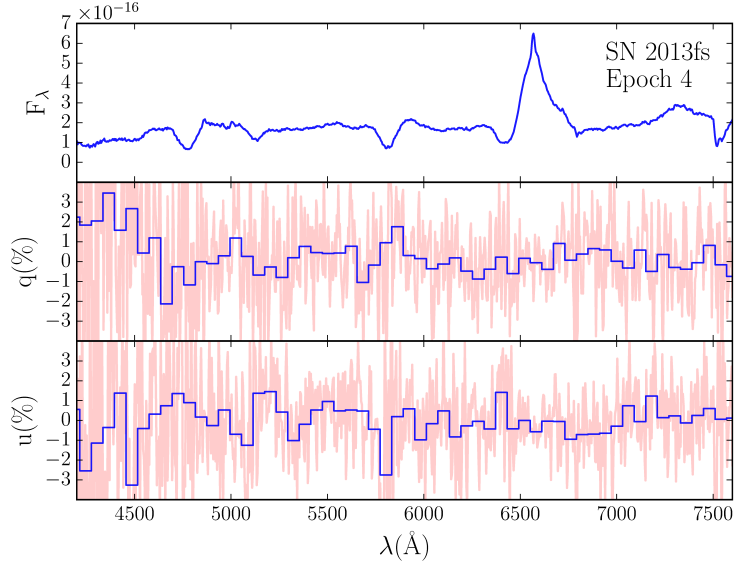


**Figure 14.** Bok spectropolarimetry of SN 2013fs, days 86 and 87 post-discovery.

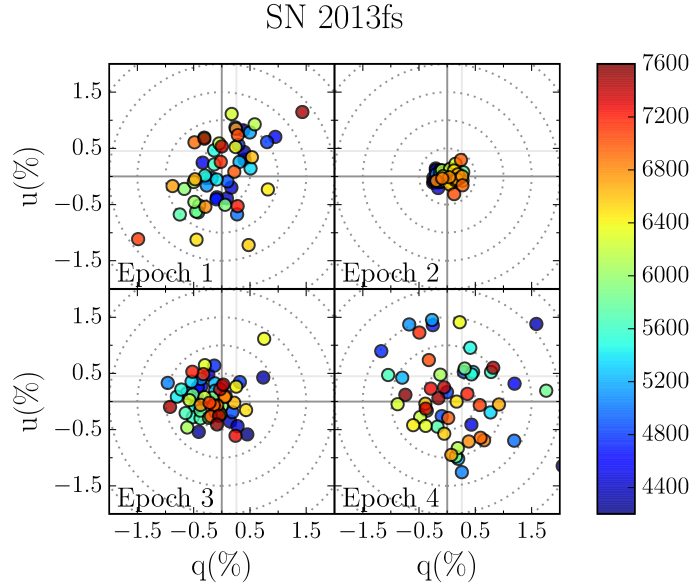


**Figure 15.** Line polarization in SN 2013fs plotted in the  $(q, u)$  plane. Points are colour-coded by wavelength ( $\text{\AA}$ ) as described in Section 3.1.4.

before ISP subtraction. Some previous studies have chosen an ISP value such that the data along a preferred axes do not pass through the origin in the  $(q, u)$  plane. This eliminates a  $90^\circ$  rotation at some point in the spectrum. However, wavelength-dependent optical-depth effects and the specific source-scatterer geometry can result in a  $90^\circ$  rotation at any

wavelength (Dessart & Hillier 2011); hence, we are not constrained by that requirement.

There is some deviation from the average in both  $(q, u)$  and  $(P, \theta)$  across the  $H\alpha$  absorption line in all epochs, but it is most pronounced in Epoch 3 (days 52 and 57), when the absorption feature is largest. This is perhaps easiest to see in the  $(q, u)$  plots in Figure 15, where the data near the  $H\alpha$

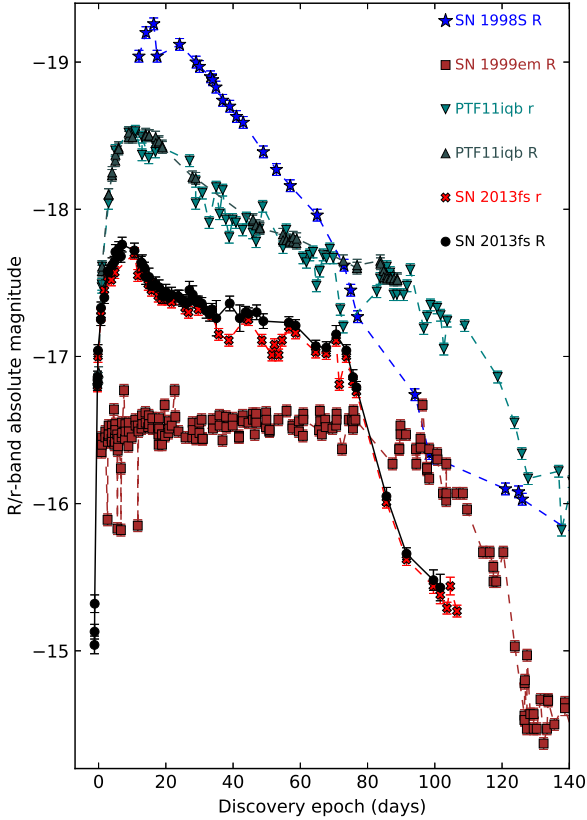


**Figure 16.**  $r/R$ -band comparison of SN 2013fs with other SNe discussed in the literature. All photometry of SN 1999em (brown; Leonard et al. 2002; Faran et al. 2014a; Galbany et al. 2016), SN 1998S (blue; Fassia et al. 2001), and PTF11iqb (teal and dark for the  $r$  &  $R$  bands, respectively; Smith et al. 2015) were retrieved from the Open Supernova Catalog. All photometry is corrected for Milky Way reddening. Days are plotted with respect to discovery, but all of these SNe were discovered within a few days of explosion.

absorption line are coloured yellow-green. This wavelength-dependent variation demonstrates that there is intrinsic SN polarization of  $\sim 1\%$ .

There appears to be a preferred axis for the continuum data in Epoch 1 that runs through the origin at approximately  $50^\circ$  and  $230^\circ$  in the  $(q, u)$  plane or  $25^\circ$  and  $115^\circ$  on the sky. In Epoch 3, that preferred axis appears to have rotated by about  $90^\circ$ , to  $140^\circ$  and  $320^\circ$  in the  $(q, u)$  plane or  $70^\circ$  and  $160^\circ$  on the sky. The data in Epoch 2 are tightly clustered around the origin, perhaps in transition from one preferred axis to the other. In Epochs 1 and 3, the  $H\alpha$  line deviates from the continuum orthogonal to the preferred axis.  $H\alpha$  in Epoch 1 is along the preferred axis for the continuum of Epoch 3 and  $H\alpha$  in Epoch 3 is along the preferred axis for the continuum of Epoch 1.

This polarimetric evolution, with a rotation of the preferred axis, isn't necessarily a result of a change in the geometry of just the scattering envelope but may be a result of a

change in the source-scatterer geometry as the photosphere recedes through the ejecta. Total continuum polarization is small ( $< 1\%$  at all epochs, and  $< 0.5\%$  at Epoch 2, where the S/N is highest. This mild asymmetry is similar to that of SN 1998S (Leonard et al. 2000; Shivvers et al. 2015).

### 3.2 SN 2013fr

#### 3.2.1 Optical and IR photometry of SN 2013fr

All photometry of SN 2013fr is plotted in Figure 5, and spectral energy distributions (SEDs) are shown in Figure 6. In contrast to SN 2013fs, SN 2013fr was caught potentially a week or more after explosion, and all optical bands are already declining by the first photometric epoch. This puts a lower limit on the true maxima of  $M_B = -18.65$  mag and  $M_V = -18.48$  mag. The decline is approximately linear in the  $BVR$ -bands, though there is a break in the photometry at about 60 days, at which point the decay slope increases noticeably in the  $VRI$ -bands, perhaps in transition to the nebular phase, though the limited temporal coverage makes this uncertain.

The slope is more shallow for the  $YJH$  filters than for the optical, with average decline slopes of  $0.05/0.04/0.03$  mag day $^{-1}$  for the  $B/V/R$  filters and  $0.02/0.02/0.01$  mag day $^{-1}$  for the  $Y/J/H$  filters, respectively. The brightness in the  $J$  and  $H$  filters is almost constant until day 63 (at which point they begin a decline similar to the break seen at optical wavelengths). At the end of coverage on day 75, all filters except  $H$  have seen a decrease of more than a magnitude. The SEDs of SN 2013fr show that an IR excess appears around day 42 and becomes prominent by day 75. The temperature decreases with time as expected, but at day 42 and thereafter the SED is well described by a double blackbody model.

After coverage ends on day 75, no point source is found in the  $gri$ -bands from the day 139 DCT photometry. Given a  $3\sigma$  limiting magnitude of  $m_r = 23.8$  mag, SN 2013fr has an average decline rate exceeding  $0.08$  mag day $^{-1}$  in the  $r$ -band, noticeably higher than the  $0.03$  mag day $^{-1}$  average  $r$ -band decline rate in the first 75 days, pointing to an accelerated decline after the end of coverage. This decline rate is consistent with, if somewhat elevated above, the later-time evolution of SNe II-L (Faran et al. 2014b). Unfortunately, no photometry was obtained during the nebular phase of SN 2013fr that would allow us to obtain a good estimate of the  $^{56}\text{Ni}$  mass. SN 2013fr is compared with several SNe II-L in Section 5.

#### 3.2.2 Spectral evolution of SN 2013fr

The spectra of SN 2013fr are plotted in Figure 9, and the  $H\alpha$  line profile is shown in the right half of Figure 10. The spectrum reddens continually with age, with relatively strong line blanketing appearing on day 28 and onward. In the final spectrum on day 69, the spectrum is dominated by the  $H\alpha$  feature, but this spectrum is noisy and most of the major SN features are unresolved. The continuum slope of the spectra changes slowly, and remains relatively blue until late times, although the apparent colour gets redder because of increased line absorption.

The day 4 spectrum of SN 2013fr is similar to

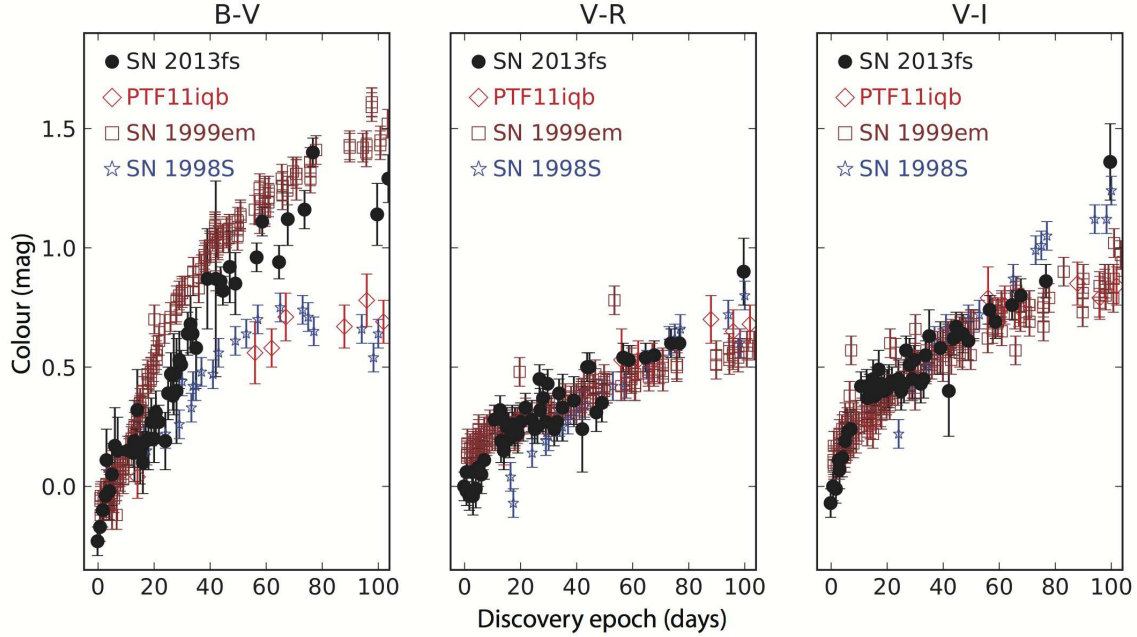


**Figure 17.** Comparative colour evolution of SN 2013fs (black), SN 1998S (blue), and SN 1999em (brown); each has been corrected for MW reddening with  $E(B - V) = 0.0347$  mag (Schlafly & Finkbeiner 2011).

that of SN 2013fs, and may contain narrow  $H\alpha$  emission attributable to the SN. The  $H\alpha$  feature develops an intermediate-width P Cygni profile and the narrow lines disappear within a few days.

The remaining narrow lines in the later-time spectra resemble those of the host, and this feature is likely to be contamination from a neighbouring H II region. In the first spectrum on day 4,  $H\alpha$  has  $EW = -24.11$  Å, while the narrow  $H\alpha$  feature at later times has  $EW > -7$  Å for all but the final epoch. Using the  $r$ -band photometry from day 12 as representative of the continuum  $F_\lambda$  on day 12, and interpolating back to day 4, the ratio of the narrow  $H\alpha$  line flux ( $EW \times F_\lambda$ ) on day 4 to that on day 12 is  $\sim 6.5$ . Host contamination may not be able to account for the much stronger narrow  $H\alpha$  emission on day 4. The P Cygni absorption velocity is variable with time, in the range 4800–5200 km s<sup>−1</sup>.

#### 4 SN 2013fs AND ITS PLACE AMONG SNe II-P & II-n

During the rise to maximum light, SN 2013fs is a close match photometrically to PTF11iqb, which is a very close spectroscopic analogue of SN 1998S (Smith et al. 2015). As seen in Figure 16, SN 2013fs has an absolute magnitude between those of SN 1999em and SN 1998S. It most closely matches PTF11iqb, but with a faster rise to maximum and a shorter, fainter plateau. The rapid rise to peak brightness is suggestive of a progenitor with an extended envelope, like a RSG. Such a progenitor was also proposed for SN 1999em, SN 1998S, and PTF11iqb; the main difference between these explosions lies in their inferred pre-SN mass loss (see Morozova, Piro, & Valenti 2017 and Smith et al. 2015).

The colour evolution of SN 2013fs (plotted in Figure 17)

tells a similar story, falling in the range between those of normal SNe II-P like SN 1999em and SNe II-n like SN 1998S. Its  $B-V$  evolution reddens quickly in the early days when the SN II-n features are still present, and after day 10 begins to slow. The  $B-V$  colour of SN 2013fs never becomes quite as red as SN 1999em, but it remains redder than either SN 1998S or PTF11iqb (Smith et al. 2015). This indicates that the blue excess, which mostly disappears by day 20, is correlated with stronger CSM interaction. After the plateau drop, the  $B-V$  colour evolution levels off. This occurs at about the same time in SN 1998S and SN 1999em, with the  $B-V$  colour of SN 2013fs remaining much closer to that of SN 1999em, consistent with the lack of CSM interaction signatures at late times.

In the redder filters, SN 2013fs mirrors SN 1999em throughout the plateau phase. After the plateau drop, the  $V-R$  and  $V-I$  colours of SN 2013fs become very red ( $\sim 0.3$  mag over that of SN 1999em in  $V-R$ , and  $\sim 0.4$  mag over in  $V-I$ ), matching SN 1998S at similar epochs.

Spectral comparisons between SN 2013fs and other SNe at early times are shown at the top of Figure 18. SN 2013fs is initially spectroscopically distinct from SN 1999em, but begins to increasingly resemble it as the plateau phase continues, and the P Cygni absorption deepens. Based on pre-explosion imaging, Smartt et al. (2002) suggested that the progenitor of SN 1999em was likely to be a RSG with an upper mass limit of  $M \approx 12 M_\odot$ . The plateau phase was shorter for SN 2013fs than it was for SN 1999em by more than a month, which usually indicates a lower-mass H envelope, and SN 2013fs has a greater decline in the  $R$  band during the plateau (SN 1999em, by contrast, has nearly constant  $R$ -band magnitude during the plateau). SN 2013fs is also almost a magnitude brighter in  $R$  for the entire duration of the plateau, conforming to the inverse correlation

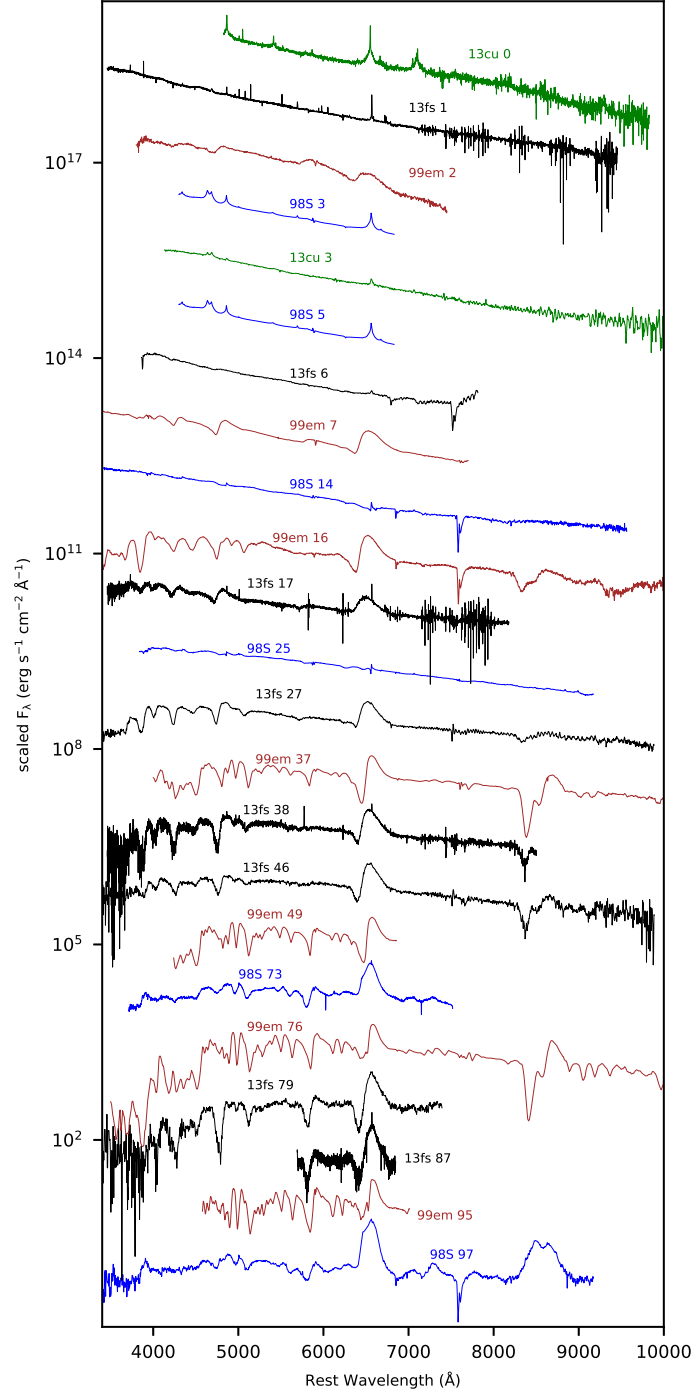


**Figure 18.** Spectra of SN 2013fs (red) compared with SN 1998S (blue), SN 1999em (brown), and SN 2013cu (green). Comparison spectra were retrieved from WISerEP. The spectra for SN 2013cu originate from [Gal-Yam et al. \(2014\)](#); SN 1998S from [Leonard et al. \(2000\)](#), [Fassia et al. \(2001\)](#), and [Fransson et al. \(2005\)](#); and SN 1999em from [Leonard et al. \(2002\)](#) and [Hamuy et al. \(2001\)](#).

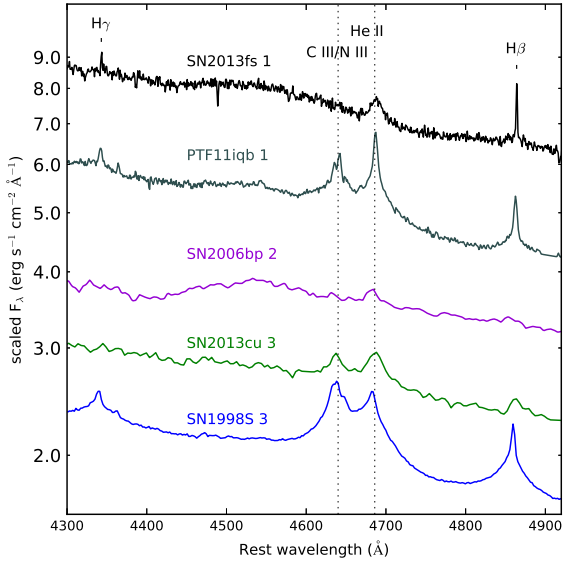


**Figure 19.** Comparison of the He II  $\lambda 4686$  and C III/N III  $\lambda 4640$  lines in SN 1913fs (black) with those of SN 1998S (blue), SN 2006bp (purple), PTF11iqb (grey), and SN 2013cu (green). The rest-frame line centres are marked by the dashed vertical lines. The spectrum of SN 2006bp is from [Quimby et al. \(2007\)](#) and that of PTF11iqb from [Smith et al. \(2015\)](#), retrieved from WISEREP. All spectra have been corrected for Milky Way Reddening.

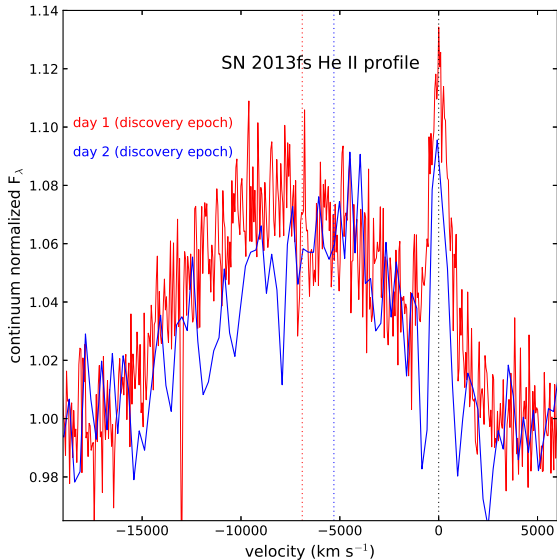


**Figure 20.** He II line profile in SN 1913fs on days 1 and 2, with the zero point on the narrow component. The dashed vertical lines indicate the line centres of the components. They have been corrected for Milky Way Reddening with  $E(B-V) = 0.0347$  mag.

between plateau decline and high peak brightness found by [Anderson et al. \(2014\)](#).

[Smith et al. \(2015\)](#) argued that the spectroscopic signatures of SNe IIn could extend to less extreme mass-loss scales or shorter durations, and that such SNe would be recognized as Type IIn only if discovered very young. SN 2013fs was discovered within 8 hr of explosion, and is an illustrative example of this phenomenon. The narrow Balmer lines produced by CSM interaction are prominent during the rise to maximum light, but quickly fade over the first two weeks, giving way to broad P Cygni profiles. The last three spectra in Figure 8 show that the broad H $\alpha$  component is slowly narrowing again at late times. The short duration of the narrow H $\alpha$  emission may suggest strong mass loss for a limited time before explosion. This conclusion is supported by the concurrent bump in the early light curve (modeled for SN 2013fs by [Morozova, Piro, & Valenti 2017](#)), and by other emission lines suggestive of CSM interaction. Since the narrow emission disappears quickly, the CSM created by this mass loss is relatively compact.

Most of the narrow features in the early-time spectrum are attributable to H II region emission, but the multi-component He II  $\lambda 4686$  feature is more interesting. The lack of other WR-like lines and the rapid fading indicates that these lines are direct probes of the CSM extremely close to the site of the explosion. The He II line has  $EW(\lambda 4686) = 3.018 \text{ \AA}$  on day 1 ( $\sim 2.5$  days post-explosion) and  $1.588 \text{ \AA}$  on day 2.58 ( $\sim 4$  days post-explosion), and is unresolved entirely in the day 4 spectrum. The He II flux ratio  $f(2.5)/f(4) \approx 2$ , following the EW ratio. Like other SNe with WR-like early features ([Khazov et al. 2016](#)), SN 2013fs has a maximum luminosity  $M_R > -17.6$  mag.

A comparison of the He II  $\lambda 4686$  and C III/N III  $\lambda 4640$  lines in SN 2013fs, SN 1998S, SN 2013cu, SN 2006bp, and PTF11iqb is shown in Figure 19. These lines typically fade within 72 hr of the first spectral epoch, as was the case in SN 2013fs. They might arise due to ionisation from the UV flash resulting from shock breakout ([Khazov et al. 2016](#)), or as the result of CSM interaction (e.g., X-rays from very early shock interaction; see [Smith et al. \(2015\)](#)). The He II emission also shows a broad, blueshifted component (plotted in Figure 20). This was also seen in SN 2006bp and to a lesser extent PTF11iqb, both of which also had plateau light curves. This component arises from the SN ejecta beneath the CSM shell, and both the broad and narrow He II vanish by day 4 (day 5.37 post-explosion), owing to shock cooling as the ejecta expand. The CSM remains important for at least a few days after these high-ionisation lines have disappeared, as indicated by the pre-plateau bump in the light curve.

Following the method of [Quimby et al. \(2007\)](#), it is possible to obtain an upper limit on the maximum distance of the shell from the SN photosphere at the moment of SBO. Based on fits to the P Cygni absorption minimum of H $\beta$  on day 17 and of H $\alpha$  on day 21, the expansion velocity of the ejecta is likely between 8400 (H $\alpha$ ) and 9300 (H $\beta$ )  $\text{km s}^{-1}$ . These later measurements are consistent with a typical early-time expansion velocity of  $\sim 10,000 \text{ km s}^{-1}$ , and the blue end of the broad He II component shows that some components of the shock underneath the CSM have expansion velocities  $\gtrsim 15,000 \text{ km s}^{-1}$ . The H $\alpha$  line ceases to be narrow some time after day 6, and the light curve enters

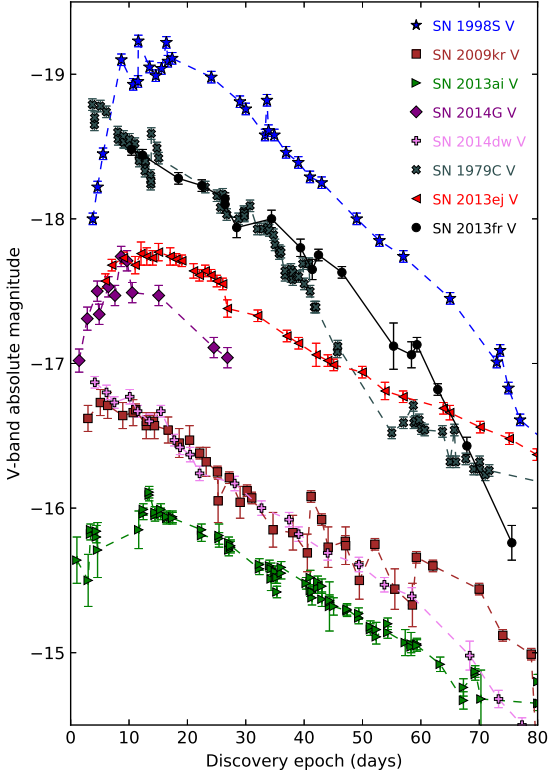


**Figure 21.** V-band comparison of SN 2013fr (black) with SN 1998S (blue), SN 2009kr (brown), SN 2013ai (green), SN 2014G (purple), SN 2014dw (pink), SN 1979C (blue-grey), and SN 2013ej (red). All photometry was obtained from the OSC, and has been corrected for Milky Way but not local reddening (if any). SN 2013ai, SN 2014G, and SN 2014dw all come from Valenti et al. (2016), SN 1979C from Barbon et al. (1982), SN 2009kr from Elias-Rosa et al. (2010), and SN 2013ej from Huang et al. (2015).

the plateau phase around three weeks later, after which SN 2013fs is photometrically and spectroscopically a normal SN II-P.

Assuming an average expansion velocity  $\bar{v}_{\text{ejecta}} \approx 10,000 \text{ km s}^{-1}$  during the initial 7.5 days post-explosion, we find the CSM to be confined within  $6.5 \times 10^{14} \text{ cm}$  ( $\sim 43 \text{ au}$  from the progenitor photosphere at SBO). If the circumstellar He II is ionised in the early-phase shock interaction, then assuming it began close to the time of our first spectrum (2.5 days post-explosion) and that the approaching ejecta below the CSM at these early phases expanded at  $\sim 15,000 \text{ km s}^{-1}$  (as measured from the blue edge of the broad He II), then the CSM shell must mostly lie beyond  $3.24 \times 10^{14} \text{ cm}$ .

The broad He II feature is absent in SN 1998S, SN 2013cu, and PTF11iqb. Since the broad feature decays quickly, its absence in these SNe may be the result of differing discovery times, or it may be blended with the strong C III/N III emission present in their early-time spectra. Of all the known SNe which exhibit WR-like lines, only SN 2006bp is also seen to have both comparably weak emis-

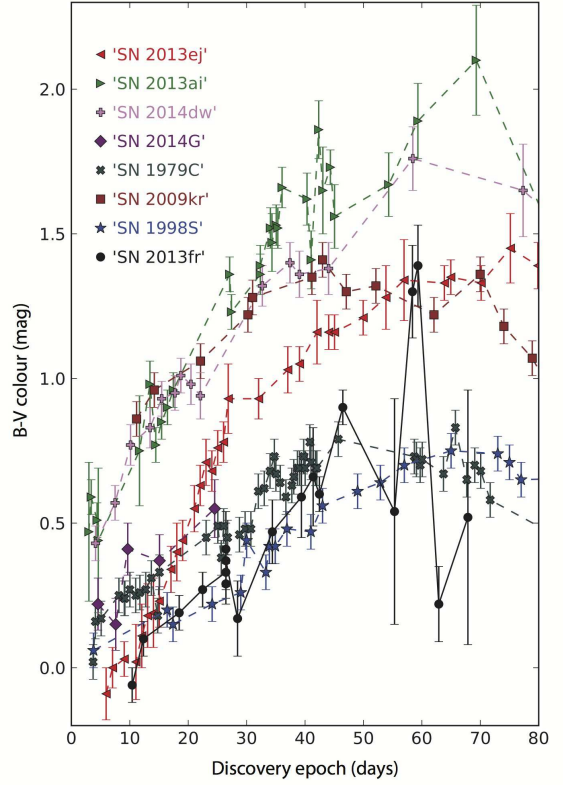


**Figure 22.** B-V colour evolution of SN 2013fr, SN 1998S, SN 2013ej, and the sample of SNe II-L.

sion of the C III/N III  $\lambda 4640$  blend and a blueshifted He II component. Interestingly, SN 2006bp has a similarly short-duration plateau like SN 2013fs, with very similar limits on the extent of the CSM shell (Quimby et al. 2007).

The nature of the mass-loss that lead to this shell and the total mass shed have been the source of a great deal of recent work. There are three recent papers which come to mostly different conclusions on one or both of these questions. Morozova, Piro, & Valenti (2017) uses the Supernova Explosion Code (SNEC; Morozova et al. 2015) with the light curves from Valenti et al. (2016), and assuming a smooth, wind-like density profile (though they suggest the phenomenon responsible could be eruptive), infers a very large amount of mass lost in a very short period of time (and consequently, a very high  $M_{\odot}$ ).

Takashi et al. (2017) use a progenitor model and radiation hydrodynamics simulations to explore the impact of wind acceleration on the duration and severity of the late stage mass-loss, finding a similar total ejected mass to Morozova, Piro, & Valenti (2017), but

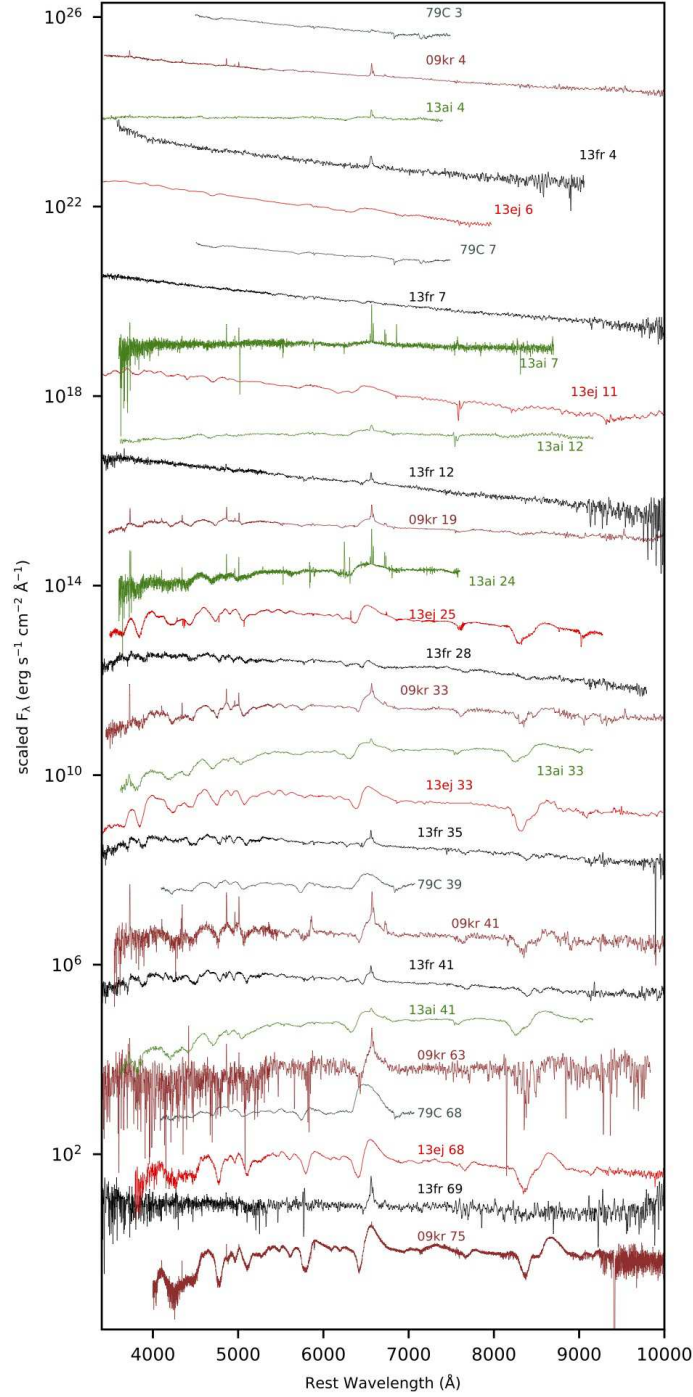


**Figure 23.** Spectra of SN 2013fr (black), compared with SN 2013ej (red), SN 1979C (grey), SN 2013ai (green), and SN 2009kr (brown). Spectral comparisons with SN 2014G and SN 2014dw were not possible owing to the lack of public spectra. All spectra with the exception of that of SN 2009kr were retrieved from WISerEP; the spectra of SN 2009kr were obtained from Nancy Elias-Rosa via email. All dates are taken with respect to discovery, and all spectra have been corrected for Milky Way reddening.

that the phase may have lasted 5–500 times longer than Morozova, Piro, & Valenti (2017) suggests, and that  $M_{\odot}$  may be as much as two orders of magnitude lower.

Yaron et al. (2017), which infers an even tighter constraint on the explosion time, uses radiative transfer modeling and extremely early time spectra to infer the pre-SN mass-loss rate. They argue for the importance of a “super-wind” phase of late stage mass-loss, and also raise the possibility of late-time eruptive events.

More recently, Dessart, Hillier, and Audit (2017) find that mass-loading in the intermediate region between the progenitor and its normal radiation-driven wind can fully account for the early signatures of interaction seen in SN 2013fs (and one of our comparison SNe, SN 2013cu), and that no transient super-wind or eruptive mass-loss phases are required at all. These will all be discussed in turn.

Morozova, Piro, & Valenti (2017) fit the photometry of SN 2013fs from Valenti et al. (2016) using a light curve model that invokes a dense CSM created by a steady-state wind, assuming spherically symmetric conditions. They determine the most likely progenitor is a RSG with  $M_{\text{ZAMS}} = 13.5 \text{--} 14.0 M_{\odot}$ , and the explosion energy to be  $E_{\text{fin}} = 0.8 \text{--} 1.0 \times 10^{51}$  erg. Using wind speeds  $v_{\text{wind}} = 10$  (100)  $\text{km s}^{-1}$ , they find the immediate pre-SN mass-loss rate of SN 2013fs to be  $\dot{M} = 0.15 M_{\odot} \text{ yr}^{-1}$  ( $\dot{M} = 1.5 M_{\odot} \text{ yr}^{-1}$ ), with an assumed outer radius of 2100–2300  $R_{\odot}$  (9.8–10.7 AU). This is higher than any known RSG wind (Smith 2014), and implies the duration of this strong wind before core-collapse is  $\sim 5$  (0.5) years. In both cases, the total mass of the ejected CSM is around 0.4  $M_{\odot}$ .

Such a high mass loss rate suggests a very late time eruptive event in the last few years (for a slower velocity outburst) or even months (for a higher velocity outburst) before core collapse. Based on the wind velocities from Table 1 of Morozova, Piro, & Valenti (2017) and the extent of the CSM shell inferred from our photometry/spectra, the mass-loss event began within 20 yr of core-collapse if  $v_{\text{wind}} = 10 \text{ km s}^{-1}$ , or within 2 yr if  $v_{\text{wind}} = 100 \text{ km s}^{-1}$ .

The mass-loss rate inferred by Yaron et al. (2017) uses the same wind velocities, but comes to much more modest values of  $\dot{M}$ . Using the He II  $\lambda 4686$  and H $\alpha$  line fluxes in conjunction with temperature fits obtained using the CMFGEN radiative transfer code (Hillier & Miller 1998), they find that  $\dot{M}$  is best fit in the range  $2 - 4 \times 10^{-3} M_{\odot} \text{ yr}^{-1}$  (using the same wind speeds as in Morozova, Piro, & Valenti (2017)); dramatically lower than that inferred by Morozova, Piro, & Valenti (2017).

Their estimate of  $\dot{M}$  scales with the wind velocity by  $\frac{v_{\text{wind}}}{100 \text{ km s}^{-1}}$ , and so even with unrealistic estimates for the wind speed (1000  $\text{km s}^{-1}$  or higher), the value of  $\dot{M}$  does not exceed about  $10^{-2} M_{\odot} \text{ yr}^{-1}$ . In addition to the early time spectra, they are also able to use later radio non-detections to rule out some longer term phases of weaker mass-loss (in the range  $6 \times 10^{-6} - 1 \times 10^{-3} M_{\odot} \text{ yr}^{-1}$ ). They do not calculate the total mass of the ejected CSM explicitly, though their calculated mass-loss rate and very short preferred timescale ( $\sim 100$  days prior to core collapse) argues for a CSM mass not much more than 0.01  $M_{\odot}$ .

Both Yaron et al. (2017) and Morozova, Piro, & Valenti (2017) assume constant wind velocities, and the values of  $\dot{M}$  and  $M_{\text{CSM}}$  in each differ

considerably. Takashi et al. (2017) drop the assumption of constant velocity, instead modeling the wind with a  $\beta$ -law profile of the form  $v_{\text{wind}}(r) = v_0 + (v_{\infty} - v_0(0))(1 - \frac{R_0}{r})^{\beta}$ , with  $R_0$  being the surface of the progenitor. Such wind acceleration models have been used for galactic RSGs in the past, and typically find  $\beta > 3$ . The same is true here, and they find  $\beta \approx 5$  provides the best fit to the early time  $r$ -band light curve.

Their model assumes that  $v_{\infty} = 10 \text{ km s}^{-1}$ , and they do not provide fits for higher values of  $v_{\text{wind}}$ . However, even for this slower wind velocity, they find that the wind acceleration model predicts that the compact CSM around SN 2013fs was lost by the progenitor within 500 years of core collapse, and possibly as little as 100 years. The total CSM mass is very similar to that found in Morozova, Piro, & Valenti (2017). For shorter mass-loss durations, like those in Morozova, Piro, & Valenti (2017) and Yaron et al. (2017), the wind acceleration model predicts that  $r_{\text{CSM}} < 10^{14}$  cm, too compact to recreate the WR-like spectral features at early times. As a result, they favour a super-wind phase starting no sooner than 550 years and no later than 100 years prior to core collapse (Takashi et al. 2017).

The most recent paper that discusses SN 2013fs, Dessart, Hillier, and Audit (2017), combines the observations of Yaron et al. (2017) with both radiative transfer modeling and radiation hydrodynamics simulations (Yaron et al. 2017, in contrast, did the former but not the latter) to find a good model of the wind/atmospheric density scale height and  $\dot{M}$ . The mass-loss values they used in their simulations range from  $10^{-6}$ – $10^{-2} M_{\odot} \text{ yr}^{-1}$ , and scale heights range from 0.1–0.3  $R_{\star}$ . Their value of  $v_{\text{wind}}$  at the outer edge of the compact CSM is 50  $\text{km s}^{-1}$ , midway between the 10–100  $\text{km s}^{-1}$  estimates used in the other papers.

Their primary interest is in the effect of the progenitor’s outer atmosphere and circumstellar material just above  $R_{\star}$  on the shock breakout and early time spectra rather than mass-loss, but they propose an alternative not considered by any of the other papers. All spatially resolved galactic RSGs have cocoons of material above the edge of the photosphere, and they propose that the compact CSM seen in SN 2013fs is attributable to the same phenomenon. In that case, there is no need to invoke a late time super-wind or eruptive mass-loss phase. Further, they challenge the “flash ionisation” interpretation of Yaron et al. (2017), Gal-Yam et al. (2014), and Khazov et al. (2016), arguing that the persistence of the WR-like lines is the result of the very high UV flux in the aftermath of the shock breakout, not the initial UV flash.

We see the spectroscopic signatures of strong CSM interaction only for the first week or so after core-collapse, whereas the photometry, well fit by the light curve models of Morozova, Piro, & Valenti (2017) and Takashi et al. (2017), shows that excess luminosity from continuing CSM interaction lasts until around 20 days post-explosion. By the time the narrow lines disappear, a week or so post-explosion, the fastest ejecta ( $v_{\text{ejecta}} \sim 10000$ – $15000 \text{ km s}^{-1}$ ) will have expanded beyond the radius of the CSM shell, causing any remnant narrow emission from continuing interaction to become obscured in the expanding ejecta. This scenario suggests asymmetry in the CSM, as was the case in PTF11iqb. Unlike PTF11iqb, where the CSM interaction re-emerged during the nebular phase as a result of more distant CSM

( $\sim 200$  AU; Smith et al. 2015), the lack of post-plateau narrow emission in SN 2013fr suggests that CSM interaction is quenched after the excess luminosity fades and the plateau phase begins.

A 0.5–100 year timescale would imply that even normal SNe II-P from RSGs experience advanced mass loss in the final stages of nuclear burning, producing SN II spectra (Smith, Hinkle, & Ryde 2009; Smith et al. 2015). The mass-loss phenomenon responsible could be a very strong, possibly accelerated super-wind, or (if the higher value of  $\dot{M} \approx 1.5 M_{\odot} \text{ yr}^{-1}$  found by Morozova, Piro, & Valenti 2017 or the 100 day timescale preferred by Yaron et al. 2017 are accurate) an eruptive event in the final stages of stellar evolution prior to core collapse (Smith & Arnett 2014; Quataert & Shiode 2012). If the mass-loss phenomenon is eruptive, then CSM velocities above  $100 \text{ km s}^{-1}$  are feasible, and the event could have happened as little as a few years before core collapse).

Only a handful of SNe are known to exhibit the spectroscopic signatures of CSM interaction, but this is likely a discovery-time problem: Khazov et al. (2016) find that they occur in as much as 18% of young SNe II, indicating that very late-stage mass-loss events may be common occurrences. On the other hand, if Dessart, Hillier, and Audit (2017) is correct and the compact CSM is nothing but an extended cocoon of surrounding material ejected earlier on, like those seen in spatially resolved galactic RSGs, the phenomenon could be near universal, and the lack of observed CSM interaction in most young SNe II-P would be attributable to variations in the density of the compact CSM. In this case, SN 2013fr and SN 2006bp represent RSGs with high density close CSM, with narrow interaction lines lasting as long as a few days (Dessart, Hillier, and Audit 2017 suggests that these lines would last at best a few hours for RSGs with tenuous CSM).

## 5 SN 2013fr: A SN II-L WITH POSSIBLE EARLY-TIME CSM INTERACTION AND LATE-TIME DUST

There is no unambiguous plateau drop observed for SN 2013fr, and all filters decline at a relatively constant rate, with the *V* band in particular dropping by  $\sim 1.3$  mag in the 45 days after our first *V*-band detection. The narrow lines disappear and reappear, but beyond possibly the first epoch, these are most likely due to changes in seeing and host contamination. Thus, we conclude that SN 2013fr is best described as a SN II-L which may exhibit early CSM interaction. Adopting a *V*-band decline of more than 0.5 mag in the first 50 days as the defining feature of SNe II-L from Faran et al. (2014b), it is a clear SN II-L. *V*-band photometric comparisons of SN 2013fr with SN 1998S, several SNe II-L (SN 1979C, SN 2009kr, SN 2013ai, SN 2014G, SN 2014dw), and SN 2013ej (an intermediate object between SNe II-P and SNe II-L; Mauerhan et al. 2016) is shown in Figure 21. SN 2013fr has a light curve similar to that of SN 1979C at early times (SN 1979C was discovered relatively young; this similarity suggests the same may be true of SN 2013fr), and it is brighter than all SNe in the sample other than SN 1979C and SN 1998S. The decline rate of

SN 2013fr is consistent with all of the well-sampled SNe II-L, and is modestly steeper than that of SN 2013ej.

The *B*–*V* colour evolution of SN 2013fr, SN 2013ej, and the SN II-L sample is plotted in Figure 22. The overall colour evolution of SN 2013fr is similar to the other SNe II-L in the sample in shape, but SN 2013fr is bluer than every other SNe II-L. It roughly matches SN 1979C in both shape and colour, and is similarly close in colour to SN 1998S. After about day 50 the points for SN 2013fr become too noisy to be certain, but if one takes the midpoint value from day 50–70, it remains very similar to SN 1979C and SN 1998S.

The spectra of SN 2013fr compared with several of the SNe II-L and SN 2013ej are plotted in Figure 23. The narrow  $H\alpha$  present in the first spectrum is similar to that in SN 2013fs. As discussed in Section 3.2.2, this feature is brightest in the first epoch, has a high EW, and the spectra do not show any other H II region features. In particular, the EW is  $\sim 6$  times larger than at any of the later epochs showing narrow H II region emission. Thus, the narrow  $H\alpha$  emission on day 4 is a potential indicator of brief CSM interaction at early phases.

SN 2013fr has variation in its P Cygni absorption speed at early times, which is atypical in SNe II-L. Of the SNe II-L with a P Cygni absorption feature, most have  $H\alpha$  velocities  $\sim 10,000 \text{ km s}^{-1}$ , with SN 2009kr having the lowest at  $v_{H\alpha} \approx 7000 \text{ km s}^{-1}$ . SN 2013fr has a P Cygni absorption speed which never exceeds  $5200 \text{ km s}^{-1}$ , with FWHM  $\approx 2200 \text{ km s}^{-1}$  after day 7, when the P Cygni absorption is resolved. The spectra of SN 2013fr best match those of SN 2009kr at similar epochs, though SN 2013fr is  $\sim 1.5$  mag brighter than SN 2009kr at all epochs. More atypical still is the variation in the P Cygni absorption minimum of SN 2013fr; it changes by at most  $\sim 300 \text{ km s}^{-1}$ . This variation is dramatically smaller than for most of the SNe II-L which show changes in their P Cygni absorption minima. Again, SN 2009kr provides the best match, as it is the only other object that shows a similar variation in its P Cygni absorption minimum of  $\sim 500 \text{ km s}^{-1}$ . These small variations, if significant, may provide additional evidence for CSM interaction in SN 2013fr and SN 2009kr.

The SEDs show an IR excess, providing evidence for dense CSM in SN 2013fr, independent of the early narrow emission lines in the day 4 spectrum. The SEDs for days 10–12, 42/43, and 75 are plotted in Figure 6. The second and third epochs show a near-IR excess that cannot be fit by a single temperature. By day 75 the contrast is substantial; the *H*-band flux is comparable to that in the *i* and *z* bands. This infrared excess can be matched by a two-temperature blackbody, with  $T_1 = 6200 \text{ K}$  (6300 K) for the SN photosphere and  $T_2 = 1200 \text{ K}$  (1500 K) for the dust in the second (third) SED. Owing to line blanketing after day 28, the *B* and *V* points fall below the blackbody curve in the second two epochs. There may, of course, also be cooler dust that is not constrained by these wavelengths.

Following Fox et al. (2011) and Fransson et al. (2013), we can calculate the evaporation radius for silicate and graphite dust grains, assuming evaporation temperatures of

**Table 1.** Evaporation radii for silicate (Si) and graphite (Gr) dust grains of size  $a$ , given the lower limit  $L_{\text{peak}} \approx 7.92 \times 10^{42} \text{ erg s}^{-1}$ , at both early times and later.

$a$ $\mu\text{m}$	$T_{\text{eff}}$ K	$R_{\text{evap}}$ $10^{17} \text{ cm}$ Silicate	$R_{\text{evap}}$ $10^{17} \text{ cm}$ Graphite
0.001	10,000	2.31	1.27
1.0	10,000	1.16	0.303
0.001	6000	0.765	0.765
1.0	6000	0.641	0.312

1500 K (1900 K) for silicates (graphites), respectively. Rearranging Equation 24 from [Draine & Salpeter \(1979\)](#),

$$R_{\text{evap}} = \left( \frac{L_{\text{peak}}}{16\pi\sigma T_{\text{evap}}^4 \langle Q \rangle} \right)^{\frac{1}{2}}, \quad (4)$$

where  $\langle Q \rangle$  is the Planck-averaged dust emissivity, and  $T_{\text{evap}}$  is the vaporisation temperature of the dust grains. Owing to the later discovery of SN 2013fr, we can only put an upper limit on  $L_{\text{peak}}$ , since the SN was already fading during the first photometric epochs. To get a lower limit on  $L_{\text{peak}}$ , we use Equation 7 from [Lyman, Bersier, and James \(2013\)](#) to obtain the  $B$ -band bolometric correction, and convert this to a luminosity.

The results are given in Table 1. Given a typical shock velocity of 10000-15000  $\text{km s}^{-1}$ , the evaporation radii for both silicate and graphite grains of sizes between 1 nm and 1  $\mu\text{m}$  lie well above the shock radius ( $R_{\text{shock}} \approx v_{\text{shock}}[t_{\text{disc}} + t_{\text{delay}}]$ , where  $t_{\text{delay}}$  is the time between explosion and discovery), assuming the explosion date was within 20 days of discovery.

Such dust could have been formed in situ after the SN explosion, or could have already been present in the CSM prior to the explosion, heated by SN light or by the forward shock. In the latter case, the dust temperature is correlated to the gas density ([Draine & Salpeter 1979](#)), and could be used to probe the mass-loss history of the progenitor. Such an IR echo results from dust absorption of optical light and subsequent re-emission at IR wavelengths. SNe IIn and Ibn commonly show IR echoes at late times when the dust is heated by the radiation from ongoing shock interaction (e.g., [Smith et al. 2009c](#); [Fox et al. 2010](#); [Mattila et al. 2008](#)), and IR echoes have been detected for decades after explosion in SN 1980K ([Sugerman et al. 2012](#)). The inferred evaporation radius of SN 2013fr renders shock evaporation of dust at these early times unlikely, if the P Cygni absorption is representative of the velocity of the forward shock. The determined dust temperatures are (especially around day 43) close to the evaporation temperature for silicate grains, so this dust could be primarily graphite.

Alternatively, if the dust does lie closer, within the ejecta, then the observed echo could still be caused by collisional evaporation of newly formed dust inside the ejecta by the reverse shock. The presence of an IR excess in SN 2013fr at such early times suggests that CSM is important in at least a subset of SNe II-L.

In principle, an IR excess could arise from newly formed dust, or an IR echo from pre-existing dust, radiatively heated by SN light or CSM interaction. Such an IR echo results

from dust absorption of optical light and subsequent re-emission at IR wavelengths. SNe IIn and Ibn commonly show IR echoes at late times when the dust is heated by the radiation from ongoing shock interaction (e.g., [Smith et al. 2009c](#); [Fox et al. 2010](#); [Mattila et al. 2008](#)), and IR echoes have been detected for decades after explosion in SN 1980K ([Sugerman et al. 2012](#)). The dust temperature in this case is correlated to the gas density ([Draine & Salpeter 1979](#)), and can be used to probe the mass-loss history of the progenitor. Given the dust temperatures in the SEDs and the luminosity of the SN on those epochs, the dust (and thus CSM from pre-SN mass-loss) is located near the evaporation radius, from 0.5-1.2  $\times 10^{17} \text{ cm}$ . This separation from the SN ejecta renders the creation of new dust at these epochs unlikely. If we assume a typical wind speed of 10  $\text{km s}^{-1}$  for this CSM, this mass-loss phase occurred between 16000 and 38000 years before core-collapse.

## 6 CONCLUSIONS & FUTURE PROSPECTS

We have presented an analysis of photometry and spectra of SN 2013fs and SN 2013fr. Owing to the good spectroscopic coverage in the first 90 days and the very early discovery time of SN 2013fs, we confirmed the presence of a dense but relatively compact CSM around the progenitor based on light curve fits and hydrodynamical models by [Morozova, Piro, & Valenti \(2017\)](#), [Takashi et al. \(2017\)](#), and [Dessart, Hillier, and Audit \(2017\)](#). The He II features in the day 1-2 spectra, along with the lack of strong CSM interaction after the beginning of the plateau phase point to a confined CSM shell in the immediate vicinity of the progenitor requiring short-duration enhanced or eruptive mass loss beginning shortly before core collapse. SN 2013fs is similar to PTF11iqb and other young SNe having WR-like spectral lines, but it is a clear SN II-P, providing a demonstration that substantial mass-loss processes in very last stages of massive stellar evolution occur in more than just the strongly interacting SNe IIn, and that there is a continuum in late-stage mass-loss rates.

The rise time to maximum brightness of SN 2013fr was undetermined owing to its later discovery relative to the explosion. The first epoch shows narrow H $\alpha$  emission possibly characteristic of CSM interaction, but this fades quickly. The lack of intrinsic narrow H $\alpha$  emission after the first epoch, combined with the linearly declining light curve of SN 2013fr, show that it is better classified as a SN II-L. The strong line blanketing after day 28 puts limits on the strength of later-time CSM interaction, and the unusual shape and low absorption minima of its P Cygni feature, almost identical to those seen in SN 2009kr, demonstrate that it was a low-velocity, possibly low-energy explosion. The IR excess that develops later is an indicator of warm dust, and a tracer of the progenitor's mass-loss history. This feature suggests that dust may be an important factor in the later evolution of SNe II-L, which are not often followed more  $\geq 100$  days post-explosion.

Short duration eruptive mass-loss has long been investigated for very massive stars due to their proximity to the Eddington limit, owing to observational evidence for variability and dense CSM ([Smith 2014](#)) in such stars. Previous work by [Yoon & Cantiello \(2010\)](#) and [Heger et al. \(1997\)](#)

showed that RSGs may also show episodes of enhanced mass-loss, which is typically not included in stellar models. Observations of galactic RSGs in the last 5-10 years suggest an increase in mass-loss toward the end of stellar evolution along the RSG branch (Davies et al. 2008, Smith 2014, Beasor & Davies 2016).

Both SN 2013fs and SN 2013fr demonstrate the importance of short-lived CSM interaction in classifying SNe. SN 2013fs, in particular, demonstrates that late-stage enhanced or eruptive mass loss and intrinsic line polarization are not limited to LBVs, and also occur in RSGs. Had SN 2013fs been discovered a week or more later than it was, the spectroscopic signatures of its close CSM would not have been detected at all. The same may be true of SN 2013fr, if the narrow emission in the first spectrum is intrinsic SN emission. More precisely determining the frequency of abrupt late-stage mass loss in the RSG progenitors of SNe II-P and SNe II-L will depend on increasing the fraction of these SNe discovered very soon after explosion. The rapid development of an IR excess in SN 2013fr suggests a CSM dust shell, the result of strong mass loss over longer timescales than the almost immediate pre-SN mass loss seen in SN 2013fs. Assessing the importance of late-time dust in SNe II-L will require a greater sample of such SNe to be monitored at IR wavelengths for more than 100 days post-explosion.

## ACKNOWLEDGEMENTS

Observations using Steward Observatory facilities were obtained as part of the observing program AZTEC: Arizona Transient Exploration and Characterization, which receives support from NSF grant AST-1515559. This paper includes data obtained by the Supernova Spectropolarimetry Project, supported by the National Science Foundation through grant AST-1210599. The SN research of AVF's group at U.C. Berkeley is supported by Gary & Cynthia Bengier, the Richard & Rhoda Goldman Fund, the Christopher R. Redlich Fund, the TABASGO Foundation, and NSF grant AST-1211916. KAIT and its ongoing operation were made possible by donations from Sun Microsystems, Inc., the Hewlett-Packard Company, AutoScope Corporation, Lick Observatory, the NSF, the University of California, the Sylvia & Jim Katzman Foundation, and the TABASGO Foundation. The Kast spectrograph at Lick Observatory resulted from a generous donation from Bill and Marina Kast. Research at Lick Observatory is partially supported by a generous gift from Google.

Some observations reported here were obtained at the MMT Observatory, a joint facility of the University of Arizona and the Smithsonian Institution. These results made use of Lowell Observatory's Discovery Channel Telescope. Lowell operates the DCT in partnership with Boston University, Northern Arizona University, the University of Maryland, and the University of Toledo. Partial support of the DCT was provided by Discovery Communications. LMI was built by Lowell Observatory using funds from NSF grant AST-1005313. We made use of *Swift*/UVOT data reduced by P. J. Brown and released in the *Swift* Optical/Ultraviolet Supernova Archive (SOUSA). SOUSA is supported by NASA's Astrophysics Data Analysis Program through grant NNX13AF35G. This work is based (in part) on observations collected at the European Organisation for Astronomical Research in the Southern Hemisphere, Chile as part of PESSTO (the Public ESO Spectroscopic Survey for Transient Objects Survey) ESO programs 188.D-3003 and 191.D-0935. Several of the spectra were retrieved from WiSEREP, the Weizmann interactive Supernova data Repository (<http://wiserep.weizmann.ac.il>). We are grateful to Isaac Shivvers and Jeff Silverman for help with one of the Lick/Kast observations and reductions. We also thank U.C. Berkeley undergraduate students/visitors Andrew Bigley, Kevin Hayakawa, Heechan Yuk, Minkyu Kim, Kiera Fuller, Philip Lu, James Bradley, Haejung Kim, Chadwick Casper, Gary Li, Samantha Stegman, Kyle Blanchard, Erin Leonard, Jenifer Gross, Xianggao Wang, Stephen Taylor, and Sahana Kumar for their effort in taking Lick/Nickel data.

We are grateful to the dedicated staffs of the observatories where data for this paper were obtained, Ryan Hofmann for his assistance with the IRAF apphot and daophot routines used in reducing the DCT/Kuiper data, and Nancy Elias-Rosa for kindly providing comparison spectra of SN 2009kr.

## REFERENCES

- Anderson J. P. et al., 2014, *ApJ*, 786, 67  
 Arcavi I. et al., 2012, *ApJ*, 756, L30  
 Barbon R. et al., 1982, *A&A*, 116, 43  
 Beasor E. R., Davies B., *MNRAS*, 463, 1269  
 Benetti S. et al., 1994, *A&A*, 285, L13  
 Bilinski C. et al., 2015, *MNRAS*, 450, 246  
 Blondin S., Tonry J. L. 2007, *ApJ*, 666, 1024  
 Breeveld A. A. et al., 2011, in *AIP Conf. Ser.* 1358, eds. J.E. McEnery, J.L. Racusin, & N. Gehrels, 373  
 Brown P. et al., 2009, *AJ*, 137, 4517  
 Brown P. et al., 2014, *Ap&SS*, 354, 89  
 Butler, N., Klein, C., Fox, O., et al., 2012, *Proc. of the SPIE*, 8446, 10  
 Cardelli J. A., Clayton G. C., Mathis J. S., 1989, *ApJ*, 345, 245  
 Childress M. J. et al., 2013, *ATEL*, 5527, 1  
 Childress M. J. et al., 2016, *arXiv:1607.08526*  
 Davies B., Figer D. F., Law C. J. et al., 2008, *ApJ*, 676, 1016  
 Dessart L., Hillier D. J., 2011, *MNRAS*, 415, 3497  
 Dessart L., Hillier D.J., Audit E., *A&A*, 605, A83  
 Draine B. T., Salpeter E. E., 1979, *ApJ*, 231, 77  
 Dressler A. et al., 2011, *PASP*, 123, 901  
 Elias-Rosa N. et al., 2010, *ApJ*, 714, L254  
 Elmhamdi A. et al., 2003, *MNRAS* 338, 939  
 Faran T., et al., 2014a, *MNRAS*, 442, 844  
 Faran T., et al., 2014b, *MNRAS*, 445, 554  
 Fassia A. et al., 2001, *MNRAS*, 325, 907  
 Filippenko A. V., 1997, *ARA&A*, 35, 309  
 Filippenko A.V., Li W. D., Treffers R. R., Modjaz M., 2001, in *Small-Telescope Astronomy on Global Scales.*, ed. B. Paczyński, W. P. Chen, & C. Lemme (San Francisco: ASP), 121  
 Foley R. J. et al., 2003, *PASP*, 115, 1220  
 Foley R. J. et al., 2007, *ApJ*, 657, L105  
 Fox O. D. et al., 2010, *ApJ*, 725, 1768  
 Fox O. D. et al., 2011, *ApJ*, 741, 7  
 Fox O. D., Kutyrev A. S., Rapchun D. A., et al., 2012, *Proc. of SPIE*, 8453, 59  
 Fransson C. et al., 2005, *ApJ*, 622, 991  
 Fransson C. et al., 2013, *ApJ*, 797, 118  
 Galbany L. et al., *AJ*, 151, 33  
 Gal-Yam A. et al., 2014, *Nature*, 509, 471  
 Ganeshalingam M., Li W., Filippenko A. V., et al., 2010, *ApJS*, 190, 418  
 Groh Jose H., 2014, *A&A*, 572, L11  
 Guillochon J., Parrent J., Margutti R. 2016, *arXiv:1605.01054*  
 Hamuy M. et al., 2001, *ApJ*, 558, 615  
 Heger A., Jeannin L., Langer N. et al., 1997, *A&A*, 327, 224  
 Hillier, D. J. & Miller, D. L., *ApJ*, 496, 407  
 Howerton S., Drake A. et al., 2013, *CBET*, 3666, 1  
 Huang F. et al., 2015, *ApJ*, 807, 59  
 Huang F. et al., 2016, *ApJ*, 832, 139  
 Khazov D., et al. 2016, *ApJ*, 818, 3  
 Komatsu E., et al. 2009, *ApJS*, 180, 330  
 Leonard D. C. et al., 2000, *ApJ*, 536, 239  
 Leonard D. C. et al., 2002, *PASP*, 114, 35  
 Lyman J. D., Bersier D., James P. A., 2013, *MNRAS*, 437, 3848  
 Mattila S. et al., 2008, *MNRAS*, 389, 141  
 Mauerhan J. et al., 2013, *MNRAS*, 430, 1801  
 Mauerhan J. et al., 2016, *arXiv:1611.07930*  
 Miller J.S., Stone R.P.S., 1993, *Lick Obs. Tech. Rep.* 66 (Santa Cruz: Lick Obs.)  
 Morozova V., Piro A.L., Renzo M, et al., 2015, *ApJ*, 814, 63  
 Morozova V., Piro A.L., Valenti S., 2017, *ApJ*, 838, 28  
 Nakano S. et al., 2013, *CBET*, 3671, 1  
 Niemala V. S., Ruiz M. T., Phillips M. M., 1985, *ApJ*, 289, 52  
 Pritchard T.A. et al. 2013, *ApJ*, 787, 157

**Table 2.** KAIT *BVRI* photometry of SN 2013fs.

$t$ (MJD)	$B$ (mag)	$\sigma_B$ (mag)	$V$ (mag)	$\sigma_V$ (mag)	$R$ (mag)	$\sigma_R$ (mag)	$I$ (mag)	$\sigma_I$ (mag)
56575.3	16.19	0.1	16.04	0.04	16.03	0.03	15.92	0.04
56576.2	16.04	0.09	16.02	0.04	15.98	0.03	15.85	0.03
56577.2	16.11	0.1	16.02	0.04	15.89	0.03	15.78	0.04
56578.2	16.18	0.14	15.97	0.05	15.87	0.03	15.69	0.04
56579.2	16.19	0.12	16.00	0.05	15.84	0.03	15.71	0.03
56585.3	16.44	0.16	16.21	0.06	15.97	0.04	15.79	0.04
56586.3	16.62	0.16	16.26	0.05	16.06	0.03	15.82	0.04
56587.2	16.54	0.10	16.36	0.05	16.06	0.04	15.86	0.05
56588.2	16.51	0.11	16.37	0.05	16.12	0.03	15.90	0.04
56589.2	16.65	0.09	16.42	0.04	16.11	0.03	15.88	0.04
56590.2	16.67	0.10	16.43	0.04	16.13	0.03	15.95	0.04
56591.2	16.77	0.07	16.46	0.04	16.19	0.03	16.01	0.04
56592.2	16.72	0.07	16.48	0.04	16.16	0.03	16.02	0.04
56596.2	16.76	0.09	16.53	0.04	16.20	0.03	16.03	0.03
56597.2	16.94	0.09	16.51	0.03	16.22	0.02	16.06	0.04
56598.2	17.05	0.07	16.54	0.03	16.24	0.03	16.06	0.04
56599.2	17.03	0.14	16.52	0.06	16.15	0.05	-	-
56600.2	17.04	0.21	16.60	0.07	16.18	0.05	16.04	0.07
56601.2	17.12	0.09	16.55	0.04	16.23	0.02	16.05	0.03
56604.2	17.26	0.07	16.58	0.03	16.29	0.03	16.10	0.04
56605.2	17.35	0.09	16.63	0.04	16.31	0.03	16.13	0.04
56607.2	17.34	0.14	16.72	0.07	16.34	0.11	16.04	0.07
56611.2	17.56	0.19	16.65	0.08	16.24	0.03	16.02	0.04
56614.2	17.54	0.38	16.63	0.15	16.34	0.08	16.18	0.10
56619.2	17.62	0.13	16.66	0.05	16.30	0.03	15.97	0.05
56621.2	17.65	0.1	16.76	0.04	16.36	0.03	16.10	0.04

- Quataert E., Shiode, J., 2012, MNRAS, 423, L92  
 Quimby R. M. et al., 2007, ApJ, 666, 1093  
 Roming P.W.A., Kennedy T.E., Mason K.O., et al. 2005, Space Science Reviews, 120, 95  
 Sanders N. E. et al., 2015, ApJ, 799, 208  
 Schlafly E., Finkbeiner D., 2011, ApJ, 737, 103  
 Schlegel E.M., 1990, MNRAS, 244, 269  
 Schmidt G. D. et al., 1992, AJ, 104, 1563  
 Shivvers I. et al., 2015, ApJ, 806, 213  
 Smartt S. J. et al., 2002, ApJ, 565, 1089  
 Smartt S. J. et al., 2015, A&A, 579, A40  
 Smith N., 2014, ARA&A, 52, 487  
 Smith N., Arnett W. D., 2014, ApJ, 785, 82  
 Smith N., Hartigan P., 2006, ApJ, 638, 1045  
 Smith N., Hinkle K. H., Ryde N., 2009, AJ, 137, 3558  
 Smith N., Owocki S. P., 2006, ApJ, 645, L45  
 Smith N. et al., 2003, AJ, 125, 1458  
 Smith N. et al., 2009c, ApJ, 695, 1334  
 Smith N. et al., 2011a, MNRAS, 412, 1522  
 Smith N. et al., 2015, MNRAS, 449, 1876  
 Sugerman B. E. K. et al., 2012, ApJ, 749, 170  
 Takashi M. J., Yoon S.-C., Gräfener G., et al., 2017, MNRAS, 469, L108  
 Valenti S. et al., 2015, MNRAS, 448, 2608  
 Valenti S. et al., 2016, MNRAS, 459, 3939  
 Wardle J. F. C., Kronberg P. P., 1974, ApJ, 194, 249  
 Watson A. M., Richer M. G., Bloom J. S. et al., 2012, Proc. of SPIE, 8444, doi:10.1117/12.926927  
 Yaron O., Gal-Yam A., 2012, PASP, 116, 326  
 Yaron O., Perley D. A., Gal-Yam A. et al., 2017, Nature, doi:10.1038/nphys4025  
 Yoon S. C., Cantiello M., 2010, ApJ, 717, L62

**Table 3.** Unfiltered KAIT photometry of SN 2013fs. Photometrically, the clear filter is similar to Johnson-Cousins R.

$t$ (MJD)	$C$ (mag)	$\sigma_C$ (mag)
56572.23	16.26	0.08
56574.23	15.88	0.03
56575.26	15.80	0.04
56575.28	15.85	0.02
56576.24	15.79	0.02
56577.24	15.72	0.03
56577.28	15.75	0.02
56578.21	15.74	0.03
56579.24	15.68	0.02
56585.25	15.89	0.03
56586.27	15.92	0.03
56587.23	15.93	0.03
56588.23	15.98	0.02
56589.22	16.04	0.03
56590.23	16.05	0.04
56592.22	16.15	0.03
56596.23	16.15	0.03
56597.21	16.18	0.02
56598.18	16.16	0.03
56599.18	16.06	0.03
56600.18	16.17	0.02
56601.18	16.20	0.02
56603.21	16.31	0.10
56604.18	16.23	0.02
56605.20	16.24	0.10
56607.17	16.28	0.03
56611.22	16.27	0.03
56612.18	16.37	0.06
56614.18	16.34	0.04
56615.18	16.57	0.20
56618.14	16.28	0.03
56619.17	16.19	0.03
56620.15	16.39	0.03
56621.17	16.39	0.03
56622.13	16.39	0.04
56623.16	16.54	0.19
56624.14	16.39	0.05
56625.17	16.43	0.04
56626.13	16.41	0.04
56627.13	16.42	0.04
56628.14	16.39	0.03
56629.14	16.37	0.04
56630.14	16.42	0.03
56631.11	16.45	0.04
56632.11	16.46	0.04
56638.14	16.54	0.05
56640.12	16.61	0.04
56642.11	16.59	0.06
56643.13	16.65	0.07
56647.14	16.69	0.07
56648.13	16.79	0.04
56650.12	16.92	0.05
56652.12	17.11	0.04
56653.11	17.17	0.06
56656.13	17.46	0.06
56658.08	17.58	0.10
56660.08	17.68	0.16
56662.10	17.97	0.13
56665.10	17.94	0.13
56674.12	18.04	0.07
56681.12	17.90	0.13

**Table 4.** Lick photometry of SN 2013fr; data come from both the KAIT and Nickel telescopes, and are listed together here. Distinct observations from within 24 hr of each other indicate a day on which SN 2013fr was observed with both KAIT and Nickel.

Time MJD	$B$ (mag)	$\sigma_B$ (mag)	$V$ (mag)	$\sigma_V$ (mag)	$R$ (mag)	$\sigma_R$ (mag)	$I$ (mag)	$\sigma_I$ (mag)
56573.4	17.02	0.02	16.93	0.01	16.65	0.01	16.49	0.02
56575.3	17.25	0.01	16.97	0.01	16.70	0.01	16.51	0.01
56581.5	17.50	0.01	17.13	0.01	16.79	0.01	16.57	0.01
56585.5	17.63	0.03	17.18	0.02	16.85	0.02	16.65	0.03
56587.5	17.77	0.28	17.25	0.19	16.95	0.13	16.74	0.21
56589.5	17.95	0.02	17.31	0.01	16.95	0.02	16.79	0.02
56589.5	17.79	0.11	16.85	0.05	16.89	0.05	16.63	0.07
56591.5	17.91	0.10	17.47	0.06	16.98	0.05	16.76	0.05
56597.4	18.15	0.08	17.41	0.05	17.08	0.04	16.71	0.04
56602.4	18.47	0.12	17.61	0.05	17.13	0.04	16.91	0.05
56604.4	18.69	0.16	17.76	0.06	17.14	0.04	16.87	0.05
56605.5	18.49	0.02	17.66	0.01	17.17	0.02	16.87	0.02
56609.5	18.94	0.03	17.78	0.02	17.28	0.02	16.94	0.02
56610.3	18.68	0.21	17.98	0.10	17.46	0.07	16.99	0.06
56618.3	19.10	0.36	18.29	0.16	17.89	0.09	17.49	0.12
56621.4	19.75	0.37	18.35	0.08	17.76	0.06	17.50	0.07
56622.3	19.94	0.12	18.28	0.03	17.67	0.02	17.36	0.02

**Table 5.** Later-time limiting magnitudes of SN 2013fs, obtained by the 61 inch Kuiper telescope, as discussed in Section 2.1.2. Late-time limits were also obtained of SN 2013fr on day 139, and these limits are found in Section 2.2.2.

Time MJD	$B$ (mag)	$V$ (mag)	$R$ (mag)	$I$ (mag)
56960	20.1	20.6	21.2	20.4
56990	20.3	20.7	21.5	20.6
57010	19.7	20.1	21.0	19.2

**Table 6.** RATIR *rizYJH* photometry of SN 2013fr. All magnitudes are reported on the AB system.

Time days	<i>r</i> (mag)	$\sigma_r$ (mag)	<i>i</i> (mag)	$\sigma_i$ (mag)	<i>z</i> (mag)	$\sigma_z$ (mag)	<i>Y</i> (mag)	$\sigma_Y$ (mag)	<i>J</i> (mag)	$\sigma_J$ (mag)	<i>H</i> (mag)	$\sigma_H$ (mag)
56570.0	-	-	-	-	16.78	0.01	16.65	0.06	16.95	0.06	-	-
56570.3	-	-	16.72	0.01	-	-	-	-	-	-	-	-
56572.0	-	-	-	-	16.83	0.04	16.64	0.06	-	-	16.90	0.25
56572.3	-	-	16.76	0.01	-	-	-	-	-	-	-	-
56573.0	-	-	-	-	16.77	0.02	16.68	0.05	16.92	0.06	-	-
56573.3	16.82	0.01	16.80	0.01	-	-	-	-	-	-	-	-
56576.0	-	-	-	-	16.88	0.04	16.68	0.05	17.02	0.06	16.88	0.22
56576.3	16.89	0.01	16.84	0.01	-	-	-	-	-	-	-	-
56579.0	-	-	-	-	16.89	0.03	16.69	0.07	17.00	0.06	17.02	0.07
56579.3	16.97	0.02	16.88	0.03	-	-	-	-	-	-	-	-
56581.0	-	-	-	-	16.87	0.01	16.71	0.17	16.99	0.06	-	-
56581.2	16.99	0.02	16.92	0.02	-	-	-	-	-	-	-	-
56584.0	-	-	-	-	16.89	0.02	16.57	0.20	16.94	0.06	-	-
56584.3	17.00	0.02	16.92	0.01	-	-	-	-	-	-	-	-
56588.0	-	-	-	-	16.93	0.02	16.64	0.19	17.04	0.06	16.96	0.05
56588.2	17.08	0.01	16.97	0.01	-	-	-	-	-	-	-	-
56590.0	-	-	-	-	16.97	0.02	-	-	17.02	0.06	-	-
56597.0	-	-	-	-	17.02	0.02	16.85	0.07	16.97	0.06	16.99	0.10
56597.5	17.21	0.03	17.06	0.03	-	-	-	-	-	-	-	-
56603.0	-	-	-	-	17.15	0.03	16.95	0.06	17.08	0.05	17.07	0.09
56603.4	17.34	0.02	17.16	0.02	-	-	-	-	-	-	-	-
56607.0	-	-	-	-	17.21	0.04	16.93	0.06	16.98	0.07	16.96	0.07
56607.2	17.42	0.02	17.24	0.03	-	-	-	-	-	-	-	-
56612.0	-	-	-	-	17.37	0.02	17.18	0.07	17.21	0.05	17.18	0.10
56612.2	17.58	0.03	17.38	0.02	-	-	-	-	-	-	-	-
56613.0	-	-	-	-	17.36	0.06	16.94	0.05	-	-	-	-
56613.2	17.62	0.01	17.27	0.02	-	-	-	-	-	-	-	-
56627.0	-	-	-	-	17.79	0.01	17.57	0.06	17.48	0.04	17.28	0.07
56627.3	18.17	0.04	17.91	0.04	-	-	-	-	-	-	-	-
56630.0	-	-	-	-	17.94	0.04	17.54	0.09	17.87	0.05	17.31	0.10
56630.1	18.30	0.01	17.98	0.01	-	-	-	-	-	-	-	-
56633.0	18.42	0.02	18.18	0.02	18.02	0.03	17.54	0.07	17.42	0.05	-	-
56639.0	18.99	0.01	18.71	0.02	18.53	0.04	18.14	0.07	18.19	0.06	17.67	0.07

**Table 7.** *Swift* UVOT photometry, taken up to day 23.6 after explosion. These data were obtained from SOUSA and reduced by Peter Brown, using a template image taken on 2016 July 14.

Time MJD	UVW2 (mag)	$\sigma_{UVW2}$ (mag)	UVM2 (mag)	$\sigma_{UVM2}$ (mag)	UVW1 (mag)	$\sigma_{UVW1}$ (mag)	U (mag)	$\sigma_U$ (mag)	B (mag)	$\sigma_B$ (mag)	V (mag)	$\sigma_V$ (mag)
56572	14.094	0.044	14.327	0.057	14.553	0.055	-	-	-	-	-	-
56573.8	14.123	0.045	14.142	0.051	14.304	0.049	-	-	-	-	-	-
56575.0	14.414	0.049	14.356	0.059	14.449	0.05	14.763	0.048	16.072	0.058	16.083	0.073
56575.9	14.817	0.055	14.776	0.064	14.661	0.053	14.829	0.049	16.093	0.058	16.04	0.072
56576.4	14.791	0.054	14.742	0.064	14.660	0.055	14.836	0.05	16.028	0.059	15.966	0.065
56577.3	15.034	0.062	14.950	0.067	14.865	0.063	14.905	0.052	16.014	0.06	15.964	0.063
56578.7	15.49	0.074	15.254	0.071	15.139	0.063	15.049	0.055	16.081	0.061	15.984	0.063
56580.1	15.773	0.078	15.599	0.079	15.43	0.069	15.132	0.058	16.114	0.064	16.02	0.078
56583.6	16.563	0.088	16.492	0.098	16.07	0.076	15.501	0.067	16.31	0.065	16.094	0.076
56584.4	16.824	0.091	16.732	0.095	16.192	0.075	15.562	0.065	16.428	0.064	16.279	0.075
56585.5	16.94	0.094	16.993	0.106	16.375	0.078	15.671	0.066	16.452	0.064	16.158	0.073
56586.4	17.155	0.099	17.142	0.11	16.552	0.08	15.776	0.066	16.514	0.064	16.294	0.074
56587.6	17.35	0.111	17.52	0.142	16.617	0.087	15.902	0.07	16.526	0.067	16.322	0.081
56588.5	17.616	0.122	17.492	0.142	16.874	0.093	15.916	0.07	16.562	0.066	16.462	0.083
56589.4	17.731	0.127	17.896	0.169	16.971	0.095	16.10	0.072	16.619	0.067	16.409	0.081
56590.5	17.95	0.139	18.149	0.195	17.172	0.1	16.143	0.071	16.587	0.065	16.443	0.079
56591.4	-	-	-	-	17.742	0.145	16.242	0.085	16.761	0.17	-	-
56592.9	18.7	0.219	18.709	0.294	17.611	0.126	16.564	0.08	16.742	0.068	16.52	0.083
56593.1	18.779	0.232	-	-	17.738	0.135	16.608	0.082	16.764	0.069	16.435	0.081
56594.7	18.946	0.259	-	-	18.146	0.169	16.723	0.084	16.866	0.07	16.572	0.085
56595.6	19.209	0.314	-	-	17.972	0.153	16.796	0.087	16.927	0.071	16.583	0.086

**Table 8.** All spectra of SN 2013fs and SN 2013fr obtained by Arizona or Berkeley observing facilities. All other spectra were retrieved from WISEREP or other online repositories of spectra. Days are given post-discovery: 2013 Oct. 7 for SN 2013fs, 2013 Sep. 28 for SN 2013fr.

Days	Telescope/Instrument	$\Delta\lambda$ ( $\text{\AA}$ )	Res. ( $\text{\AA}$ )	SN
4	Kuiper/SPol	3850–7800	3.95	2013fs
5	Kuiper/SPol	3900–7900	3.95	2013fs
6	Kuiper/SPol	3850–7800	3.95	2013fs
21	MMT/SPol	4000–7050	2.47	2013fs
23	MMT/SPol	4000–7050	2.47	2013fs
52	Bok/SPol	3850–7800	3.95	2013fs
57	Bok/SPol	3850–7800	3.95	2013fs
86	Bok/SPol	3860–7800	3.95	2013fs
87	Bok/SPol	3860–7800	3.95	2013fs
87	MMT/BlueChannel	5690–6850	0.43	2013fs
7	Lick/Kast	3350–10,250	1.96	2013fr
12	Lick/Kast	3350–10,250	1.96	2013fr
28	Lick/Kast	3350–9800	1.96	2013fr
35	Lick/Kast	3350–10,250	1.96	2013fr
41	Lick/Kast	3380–10,380	1.96	2013fr
46	Magellan/IMACS	5280–9460	1.46	2013fr
69	Lick/Kast	3370–10,380	1.96	2013fr

This paper has been typeset from a  $\text{\TeX}/\text{\LaTeX}$  file prepared by the author.